Experimental Features of Hyperon-Nucleon Interactions

Nicholas Hadjigavriel

Master of Science by Research

University of York

School of Physics, Engineering and Technology

December 2023

Abstract

This thesis presents the study of the hyperon-nucleon scattering interactions of $\Sigma^- p \rightarrow \Sigma^- p$ and $\Sigma^+ p \rightarrow \Sigma^+ p$ using data from the g12 experiment performed at the Thomas Jefferson National Accelerator Facility. Shedding light on these interactions will allow physicist to obtain a more clear description of the dynamics of hyperons in the core of neutron stars. This will subsequently allow the refinement of the Equation of States of Neutron stars and the resolution of the "Hyperon Puzzle".

The two scattering interactions were investigated in conjunction through the determination of their cross section ratio. The cross section ratio of the two reaction were calculated as a function of both momentum and energy, and finally compared to the cross section ratio calculated using the Clebsch-Gordon coefficients of the Isospins.

This work established a promising preliminary agreement between experimental cross section ratios at low momenta and theoretical predictions based on Clebsch-Gordon coefficients. This initial result serves as a crucial stepping-stone for future investigations, laying the groundwork for more accurate extraction of cross section ratios in subsequent studies that will enhance the collaborative work of experimentalists and theorists in the attempt of solving the "Hyperon Puzzle".

Disclaimer

I declare that this thesis is a presentation of original work and I am the sole author. This work has not previously been presented for a degree or other qualification at this University or elsewhere. All sources are acknowledged as references.

Contents

1 Introduction

1.1 The Atom

The emergence of the atom finds its origins in ancient Greece. Philosophers such as Democritus and Aristotle believed in the existence of an indivisible fundamental particle of which nothing smaller can exist. The name atom comes from the Greek word atomo which translates to "uncuttable" [1].

It was not until 1897 when J.J. Thompson discovered the first subatomic particle, the electron, and changed forever the perception that the atom was the smallest building block that made up the Universe. While experimenting with cathode rays, Thompson realised that these were made up of negatively-charged particles. On top of that, from the magnitude of the deflection of the aluminium plates that were incident with the cathode rays, Thompson was able to determine the mass-to-charge ratio for this new particle. To his astonishment, he found the mass of the electron to be 1/1,836 that of the mass of a hydrogen ion [2].

From his findings, Thompson came to a conclusion in 1904, that at last the atom was not indivisible, dismantling the old idea. He proposed the famous "plum pudding model" of the atom, where the atom is made up of a sea of electrons surrounding a uniform positively charged sphere, therefore cancelling out the negative charge of the electrons, giving rise to the neutral state of the atom [3]. The discovery of the electron sparked the journey of the discovery of fundamental particles of nature.

It wasn't until 1911 that Thomson's model lasted before it was nullified by one of his students, Ernest Rutherford. Through a scattering experiment on a gold-foil, Rutherford provided evidence that the atom is made up of mostly empty space, with a tiny but massive positive nucleus located at the centre of the atom, with negatively charged electrons orbiting the nucleus [4].

The issue with Rutherford's model that prevented it from lasting was the fact that electrons (or any charged particle) that experience orbital motion would emit electromagnetic radiation, dissipating an amount of their energy, and in return would spiral towards the nucleus, thus making Rutherford's model unstable [5].

It was yet another great scientist, by the name Neils Bohr that two years after Rutherford, proposed the idea that the electrons orbiting the nucleus of the atom, have allowed, discrete, energy states and fixed orbits. Bohr postulated

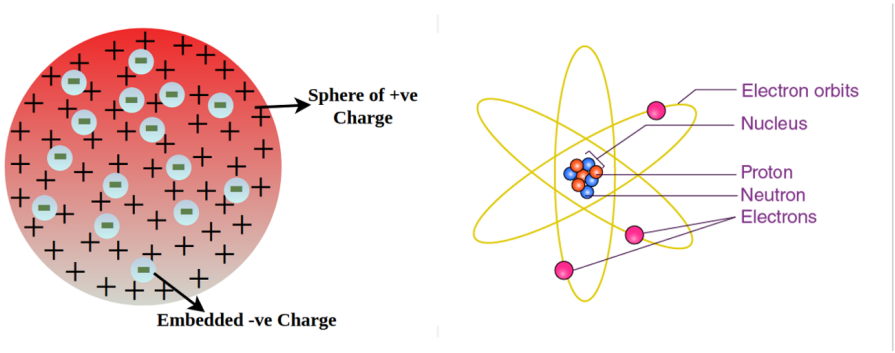

Figure 1: (Left) : J.J. Thompson's plum pudding model, (Right) Rutherford's nuclear model.

that the emission or absorption of electromagnetic radiation by an atom occurs due to electrons jumping between different discrete excited or ground states [6]. Experimental evidence of discrete energy levels, that supported Bohr's model, were obtained three years later by James Frank and Gustav Hertz [7].

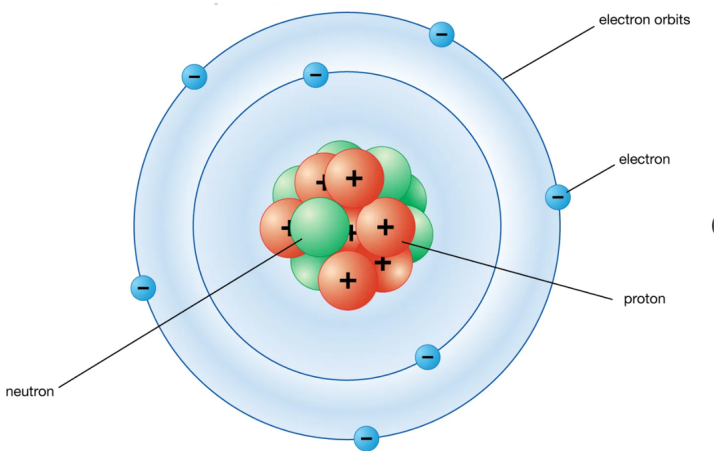

Figure 2: Bohr's model [8].

Today most textbooks employ the nuclear shell model, which is based on work of Dmitri Ivanenko (1932) together with the independent work by Eugene Paul Wigner, Maria Goeppert Mayer, and J. Hans D. Jensen, who shared the 1963 Nobel Prize in Physics for their contributions [9].

In the nuclear shell model, nucleons are arranged in a similar fashion that electrons are arranged in the atomic shell model. Within the nucleus, protons

and neutrons are arranged in orbital shells, the discrete energy of which corresponds to the energy difference between nuclear orbits [10].

1.2 Standard Model

From the 1930's and onward, scientific theories and discoveries on particle physics, quantum mechanics, and theoretical physics provided a deep understanding in the fundamental aspects of the universe. The best formulation of these remarkable discoveries lies within the Standard Model [11].

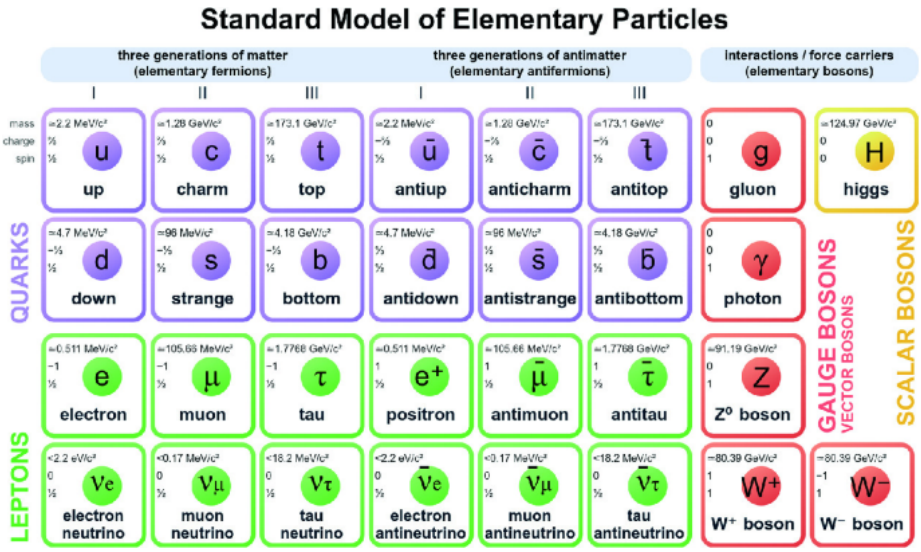

Figure 3: The Standard model of elementary particles. [16]

The Standard Model is the theory that encapsulates the elementary particles that compose all matter in the universe, along with four fundamental forces that govern all interactions between them. Each fundamental force comes with its own fundamental force carrier that mediates the particular interaction. The four fundamental forces and their associated gauge boson are the Electromagnetic force mediated by the photon, the Strong force, which is conveyed by the gluon, the weak force born by the W and Z bosons, and Gravity with the hypothetical graviton as its mediator [12].

Particles in the Standard Model lie within two families: those of fermions and bosons. Bosons comprise the aforementioned charge carriers as well as the recently discovered Higgs Boson. Fermions are split into two subgroups, of

quarks and leptons [13].

1.2.1 Quarks

The discovery of the quark is thought to be one of the greatest accomplishments in physics. It started in 1964 with the work of Murray Gell-Mann and George Zweig who independently hypothesised the existence of quarks as part of their work on the symmetries of particles. Experimental evidence for the existence of quarks only became available in 1968 with deep inelastic scattering experiments at the Stanford Linear Accelerator Center.

There exist six different flavours of quarks named up (u), down (d), strange (s), charm (c), bottom (b), and top (t) for which experimental evidence for all different flavours of quarks were not available until 1995 [14]. Quarks come also in three different colour confinements of red, blue, and green. The colour assignment of quarks in hadrons is an intrinsic property of the quark and it explains a particles' strong interactions within the theory of quantum chromodynamics (QCD). The quarks that make up a meson or a baryon must be of different colour [15].

A quark is an elementary particle and the smallest component of matter. In the previous sentence I referred to the quark in singular, which is something that never occurs in nature, since quarks only exist in combinations with each other in hadrons, such as protons and neutrons. This is due to the colour confinement of quarks.

1.2.2 The Strong Force

The theory of quantum chromodynamics (QCD) depicts the strong force within the aspects of the standard model. In QCD theory, attraction exists between quarks of different colour as a result of the strong force, the same way that particles of different electric charge are attracted to each other as a result of the electromagnetic force.

Until the 1970's it was not clear how nucleons were held together inside the nucleus. The presence of the neutral neutron, and the absence of a negative nucleon meant that positively charged protons would repel each other causing the nucleus to fall apart. The existence of an attractive force, stronger than the electromagnetic was suggested to oppose the effects of electromagnetic repulsion between nuclei. Consequently, the strong force got its name from the fact that it is the strongest of all the other fundamental forces [17].

1.2.3 Hadrons

As previously mentioned, the force carrier for the strong force is the gauge boson gluon. However, this is the case when we examine strong interactions at the smallest scale, between quarks that make up hadrons.

When it comes to larger distances, such as the separation between nucleons in a nucleus, the influence of the strong force mediated by gluons, which is responsible for binding quarks within protons and neutrons, diminishes. In the case of nucleons, the strong nuclear force is mediated by mesons. A meson is one of the two types of hadrons (the other being baryons) , and it is made up of one quark and one antiquark. Baryons are made up of three quarks. The exchange of mesons results in a nuclear force strong enough to overcome the electromagnetic repulsion between protons.

Hadron research is a highly active research area, within the particle physics community. Many current facilities (e.g LHC at CERN) collide hadronic particles with each other and collect the remains, which are known as the particle shower. A particle shower, is the name given to subsidiary particle interactions produced when a high-energy particle interacts with dense matter [18].

The use of high-energy accelerators and high sensitivity detectors, such as CERN and JLab, has been providing valuable insights to the properties of hadrons and their interactions via the fundamental forces. Furthermore, since 1950's, particle colliders have been verifying the existence of excited states of baryons and mesons as well as the discovery of exotic hadrons. Exotic hadrons in contrast to ordinary hadrons, contain more than three valance quarks [19].

Experiments are actively carried out in order to discover new excited states, and to verify the existence of exotic hadrons.

1.2.4 Strangeness

Strangness is a intrinsic property of hadrons that carry strange quarks. The name was attributed due to the strange behavior observed during research on high-energy cosmic rays research. The newly found pion and Kaon mesons, seemed to instantly appear into existence, but took their time to decay, despite their large masses and large cross-sections [20]. To explain this strange behaviour Gell-Mann proposed that another fundamental property must exist, which he named strangeness, that is conserved during the creation of these particles but not conserved during their decay. Essentially, strangeness is conserved in events governed by the strong force and not conserved in those governed by

weak interactions [21].

The strange quark was one of the first quarks to be postulated by Gell-Mann. It is the only quark with a non-zero strangeness. This indicated that Kaons and Lambda baryons observed must contain a strange quark, making them a special type of baryons, hyperons.

1.3 Hyperons

A hyperon is a baryon that is made up of at least one strange quark, and no charm, top, or bottom quarks. Most of the times hyperons are more massive than nucleons due to the fact that the strange quark that they contain, is heavier than the up and down quark.

Evidence for Hyperons was first introduced by Louis Leprince-Ringuet in 1953, through his experiments with cosmic rays. Since then, hyperon physics have been a highly researched area of physics, with experiments dedicated to the subject, in a number of facilities around the world such as CERN, Fermilab, SLAC, JLAB, Brookhaven National Laboratory, KEK, GSI and others [22].

The strange quark(s) of hyperons, results in hyperons experiencing strangeness i.e., they are created by the strong interaction but decay via the weak interaction, making them unstable. Even though their decay takes far more time than their creation, when taking into consideration terrestrial conditions their decay time is so short that direct detection of hyperons is impossible. A more stable state of hyperonic matter might exist in extremely dense and hot conditions, such as those that exist in the core of neutron stars [23].

1.4 The "Hyperon Puzzle" of Neutron Stars

Neutron stars are some of the most astonishing objects in the universe. Essentially, neutron stars are the remains of the collapsed core of supergiants, after a supernova explosion. With masses of 1.4 solar masses and radii of 10 km, neutron stars are some of the most dense objects in the universe. Attempting to grasp how dense a neutron star is someone should imagine that a neutron star the size of a matchbox would have a mass of 3 billion tonnes [24].

The first evidence for the existence of neutron stars came when Jocelyn Bell observed a pulsating signal, which later was deduced to be a pulsar i.e., a highly magnetized rotating neutron star that emits beams of electromagnetic radiation out of its magnetic poles [25]. Many more neutron stars were observed since

1967, but internal conditions within their core have not yet been defined with certainty.

The core of a neutron star is so dense, that it is unavoidable for protons and neutrons to decay into heavier baryons i.e., hyperons, as additional degrees of freedom are expected to emerge. The high density creates an environment where the strong force between quarks is great enough to overcome the energy cost of creating strange quarks. Therefore, the appearance of strange quarks becomes more energetically favoured rather than ordinary nucleons (protons and neutrons) [26].

The presence of hyperons in neutron stars creates a contradiction between theoretical models of neutron stars and observational evidence. As a result of additional degrees of freedom, the neutron star Equation of State (EoS) become softer. The term softer simply means that there is a smaller than expected, increase in the degeneracy pressure of the core with an increase in density, causing the neutron star to be more compressible, as the pressure can no longer compensate for the gravitational field [27]. A more compressed neutron star implies that a neutron star of given mass will be constrained within a smaller radius. Therefore, the maximum allowed mass that a neutron star can reach before collapsing is reduced, to a value of approximately 1.5 solar mass, but observational evidence of pulsars J1614-2230 and J0348+0432 with masses of 2 solar masses, disagree with the current hyperonic neutron star models [28].

1.5 Experimental Motivation

To resolve the "Hyperon Puzzle" the maximum allowed mass from the theoretical models of hyperonic neutron stars should increase, and for this to happen, reforming of the EoS is necessary. A stiffer equation of state (where the pressure increases a lot with a given increase in density) must be established that will counter the strong interactions that result in softer EoS. For this to be accomplished, a repulsive interaction between hyperons must be established in order to stiffen the EoS. However, to do this we first need to examine further the interactions between hyperons and neutrons.

Currently, the experimental constraints on the theoretical descriptions of hyperon-nucleon interactions are very limited. This is primarily due to the fact that hyperons are very unstable, and will decay very rapidly after their creation. This prevents the existence of lived/stable beams or targets to perform high precision scattering experiments. As a result the performance of high precision

scattering experiments involving hyperons is hindered.

This research analysis presents a novel approach to access the interaction between hyperons and nucleons, allowing us to explore this interaction in unprecedented detail. The ultimate goal of the project is to determine the experimental cross section ratio of the scattering reactions $\Sigma^+ p$ and $\Sigma^- p$. Additionally, the project aims to provide a theoretical determination of the cross section ratio of the scattering reactions. Precise experimental measurements can aid in constraining and refining the underlying dynamics of the hyperon nucleon interaction.

1.5.1 The Reaction

Scattering experiments are required to investigate the interaction of hyperons and nucleons. However, due to the short lifetime of hyperons, establishing precision measurements with hyperon beams or targets is quite challenging. To overcome this difficulty, we perform scattering experiments of hyperons with nucleons, which result in subsidiary reactions and particles that can be detected by modern-day detectors.

The 2021 CLAS Collaboration research paper "Improved Λp Elastic Scattering Cross Sections between 0.9 and 2.0 GeV as a Main Ingredient of the Neutron Star Equation of State" constituted the first examination of this reaction since 1970s. The new cross sections not only exhibited significantly improved accuracy and precision compared to existing data, but also laid the groundwork for future experiments [29].

This subsequent work will expound upon these findings, offering a comprehensive analysis of the scattering of another hyperon, Σ^-, thereby contributing to our broader understanding of hyperon physics.

The Hyperon-nucleon interaction that this research was dedicated on is the photodisintegration of a proton target. This reaction produces a positive Kaon and Lambda-1405. The Λ1405 particle has a very short lifetime and will thus decay into a Σ^- and a π^+ or a Σ^+ and a π^- before being detected by the detector(see Fig. 4).

$$\gamma p \rightarrow K^+ + \Lambda(1405) \tag{1}$$

$$\Lambda 1405 \rightarrow \Sigma^- + \pi^+ \tag{2}$$

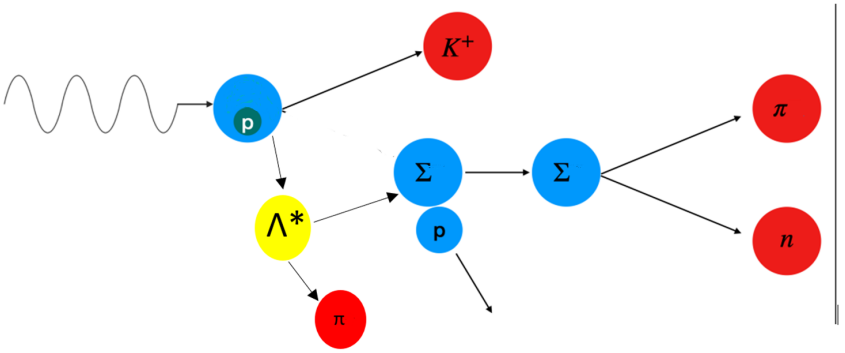

Figure 4: Schematic diagram of the reaction of interest. The reaction begins as a photodisintegration reaction of a proton target. This will result in the photoproduction of $\Lambda(1405)$ and K^+. The $\Lambda(1405)$ decays rapidly into a Σ^- or a Σ^+ and a π^+ or π^- respectively. The Σ baryon will then undergo elastic scattering with a proton, and eventually decay into a pion and a neutron.

or

$$\Lambda 1405 \rightarrow \Sigma^+ + \pi^- \tag{3}$$

The Σ^- will then undergo elastic scattering by hitting a proton, before decaying into a neutron and a π^-.

$$\Sigma^- p \rightarrow \Sigma^- p \tag{4}$$

$$\Sigma^- \rightarrow \pi^- n \qquad \frac{\Gamma_i}{\Gamma} = 99.848 \pm 0.005\% \tag{5}$$

In a similar reaction the Σ^+ undergoes elastic scattering with a proton before decaying into a neutron and a π^+.

$$\Sigma^+ p \rightarrow \Sigma^+ p \tag{6}$$

$$\Sigma^+ \rightarrow \pi^+ n \qquad \frac{\Gamma_i}{\Gamma} = 48.31 \pm 0.30\% \tag{7}$$

The neutron is not detected in the current work due to the fact that the CLAS detector has a low efficiency for detecting neutral particles. Therefore, requiring the detection of the neutron would have reduced the statistics of the reaction significantly. Overall, the four particles that are detected are K^+, π^+, π^-, and a proton.

2 The Experiment

The experimental data that were utilised in this project were gathered at the Thomas Jefferson National Accelerator Facility (TJNAF). Located at Newport News, Virginia, the Jefferson Laboratory (JLab), as it is widely known, is a leading U.S. Department of Energy nuclear physics research centre, which is actively used by the international scientific community due to its cutting edge technology. JLab is made up of the Continuous Electron Beam Accelerator Facility (CEBAF) and four experimental halls. A,B,C, and D.

2.1 CEBAF

The Continuous Electron Beam Accelerator Facility (CEBAF), at JLab, is designed to generated polarized electrons beams, that help researchers to explore the physics behind the structure of quarks and gluons that comprise nucleons and mesons. The CEBAF structure and composition allows for the high-quality electron beams to be distributed to the four different experimental halls at the same time with energies up to 12 GeV. However, when the g12 experiment was running it was able to generate electron beams up to 6 GeV and only halls A,B, and C existed back then. The accelerators racetrack shape together with its non-resistive and superconducting radio frequency (SRF) cavities allow electrons to be delivered directly to Hall B. The continuous beam is essentially made up of groups of electrons with a time separation of 2 ns. The beam currents during the g12 experiment were between 70 to 130 nA. A three-laser GaAs photocathode system was used to generate the electrons. The electrons were then accelerated with superconducting radio frequency (SRF) cavities operating at 499 MHz. The electrons pass through the tube before going through the SRF linear particle accelerators (LINACs) five times. LINACs is made up of twenty cryomodules. Each cryomodule accommodates eight superconducting niobium cavities. To continuously accelerate electrons, the LINACs generate a standing electromagnetic wave inside the niobium cavities (see Fig. 5). Every time an

electron moves through the accelerator, it obtains an additional energy of 1.2 GeV (or 600 MeV for each LINAC). The g12 experiment used electrons with a maximum energy of 5.7 GeV to produce tagged photons with a maximum energy of 5.4 GeV in Hall B. The accelerator has been modified recently to accommodate 12 GeV electrons into Hall B, which is now known as CLAS12 [30].

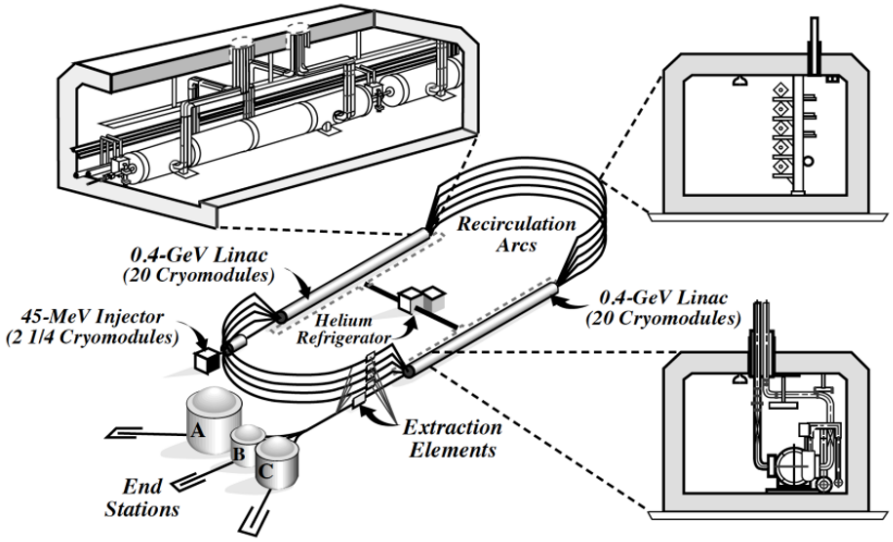

Figure 5: Schematic diagram of CEBAF [30].

2.1.1 CLAS

The design of the CEBAF Large Acceptance Spectrometer (CLAS) centers around a toroidal magnetic field that allows the high resolution measurement of the momentum of charged particle products, and for their geometrical coverage at large angles in the laboratory. The particle detection system of CLAS is made up of drift chambers for determining charged particle trajectories, Cherenkov counters for identifying electrons, scintillation paddles for measuring time-of-flight (TOF), and electromagnetic calorimeters for detecting showering particles. Six superconducting coils are positioned around the beam line to produce a magnetic field which is directed in the ϕ direction (see Fig. 6). Individual segments are equipped to form six essentially independent magnetic spectrometers with a shared target, trigger, and data-acquisition (DAQ) system.

2.1.2 Tagger System

In general, CEBAF is able to directly deliver electrons to the target. The g12 experiment is instigated by photoproduction and therefore instead of using an electron beam, a photon beam is used. The electron beam from CEBAF strikes a radiator, which is a target made from a very thin gold foil producing photons by the bremsstrahlung process that interract with a hydrogen target in the centre of the spectrometer. The electrons then pass through a dipole magnet that bends their path away from the beam-line so that the only particles that will arrive at the proton target will be neutral particles. The last part of the process is known as "photon running". The electron that are travelling away from the target are eventually detected by scintillator hodoscopes, known as electron taggers. The electron taggers are made up of two different counters. The E-counters that are responsible for measuring the energy of the electrons, and the T-counters that measure that record timing information [31]. The latter allows us to correlate events detected in a large acceptance spectrometer with a photon, whereas the former allows us to identify (tag) the energy of the photon.

2.1.3 Start Counter

Photons are directed towards the center of CLAS, where a Deuterium or Hydrogen target awaits them. The interaction of photons with the target produces a variety of reactions that can be studied in detail using the various sub-components of CLAS.

The first component that is used in photon induced experiments is the Start Counter (SC). Immediately after their creation, the products of the photodisintegration reaction arrive at the Start Counter. There are four scintillator paddles in each of the six sectors of CLAS connected with photo-multiplier tubes. These 24 scintillator paddles surround the target within the acceptance of the drift-chambers. The Start Counter is responsible for detecting charged particles and recording their time. The event start time was then established using timing information from the RF beam bunch, and was used to match the product particles with the photon detected by the tagger system that instigated their creation [32].

2.1.4 Torus Magnet

The use of a superconducting toroidal magnetic field together with the detector subsystem of Drift Chambers (DC), allow researchers to obtain the momenta of charged particles. The six coils separate the drift chambers into six areas known as Regions (see Fig. 6). The individual coils are made up of 4 layers of 54 turns of aluminum-stabilized NbTi/Cu superconductor, that were initially cooled to a temperature of 4.5 K. The Six superconducting coils, positioned around the beam line, produce a toroidal magnetic field. The magnetic field is directed so that positively charged particles are bent away from the beamline, while negatively charged particles are bent towards the beamline [33].

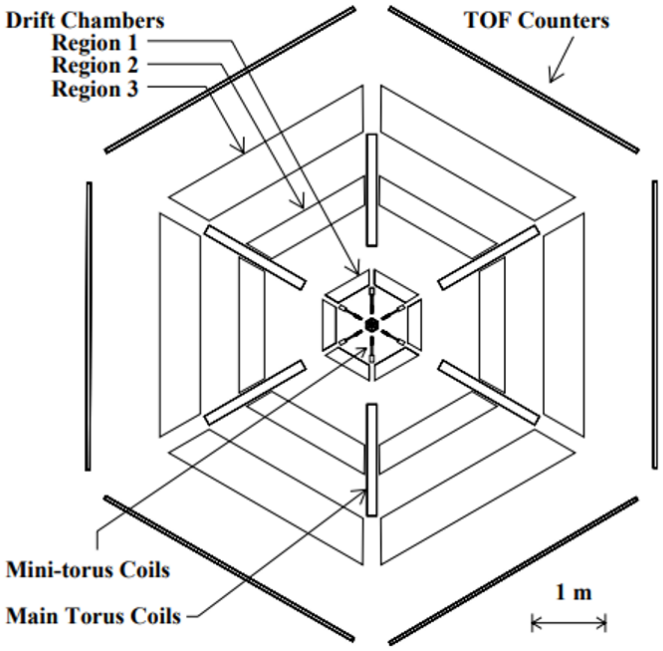

Figure 6: A schematic illustration of the CLAS detector with a cut perpendicular to the beam. The Main Torus made up of the six superconducting coils can be seen separating the DC into six Regions. The mini-torus, which is exclusively utilised during electron runs, is also shown. [30].

2.1.5 Drift Chambers

Drift Chambers are responsible for measuring the curved trajectories of charged particles by the in-bending and out-bending magnetic field to determine their momentum. Made up of three regions in each of the six sectors, drift chambers make up the primary detector subsystem of CLAS. Each region consists of two superlayers containing six layers of wires. These wires are made from 20μm gold-plated tungsten "sense wires" with a constant moderate positive voltage. Surrounding the sense wires, the six high negative voltage 140 μm gold-plated aluminum alloy "field wires" can be found. The gas chamber is filled with 90% argon and 10% carbon dioxide gas (non-flammable), allowing for the ionization of the gas particles. The ionised electrons cascaded towards the sense wires, generating a signal that was amplified and recorded by the on-board electronics. The DC system's distinctive shape not only ensured high acceptance at CLAS, but also allowed for good tracking resolution and efficiency [33].

2.1.6 Time-of-flight Counters

The "time of flight" of the charged particle exiting CLAS are given by the coordination of the time-of-flight counters, that record the Stop time of the charged trajectories, and the Start Time given by the aforementioned Start Counter. Using the path length measured by the drift chambers the velocity of the particle, β, can be found. Using the known masses of the particles the momentum can be found and in turn particle identification can be successfully performed.

2.1.7 Cherenkov Counters

Between the drift chambers and the Time-of-flight Counters the Cherenkov Counters can be found. They are responsible for differentiating electrons and pions. When an electron passes through these detectors, it emits Cherenkov radiation, which traverses through the perfluorobutane gas. Pions with momentum below 2.5 GeV do not emit Cherenkov radiation. At the same time, electrons have a threshold momentum of 9 MeV, which makes them easy to distinguish from pions, with a 97% detection efficiency [34]. This subsystem was not used during the g12 experimental run, but this system is crucial for electroproduction experiments.

2.1.8 Electromagnetic Calorimeters

Electromagnetic calorimeters (EC) are used to detect neutral particles outside of the TOF system. The EC is made up of a succession of scintillators and lead sheets situated on photomultiplier tubes. The interaction of neutral particles with the lead sheet results in the emission of radiation that is magnified by a scintillator sheet. This process is continued through multiple layers of lead and scintillators until the produced photons reach the photomultiplier tubes, where they can be converted into an electrical current. The detection efficiency for neutral particles is relatively low and for that reason the signal from the EC was not used in this analysis [35].

3 Event Selection

As previously stated, the reaction produces a positive Kaon (K^+) and Lambda-1405 (Λ-1405). The Λ-1405 particle, has a very short lifetime ($6.59 \times 10^{-24} s$), decays into a $\Sigma^{\pm}$ and a $\pi^{\pm}$ without being detected by the CLAS detector. In this analysis, events where $\Sigma^{\pm}$ undergoes elastic scattering with a proton target,were selected. The Σ baryon subsequently decays into a neutron and a $\pi^{\pm}$. In this particular experiment neutral particles were not detected by CLAS, and thus the neutron remains undetected. In total, four particles are detected: K^+, π^+, π^-, and a proton.

3.1 Skimming

The primary goal of skimming is to keep the relevant bits of data, and remove unnecessary events. initial skimming is done by selecting events with 3 positive and 1 negative. This criteria alone significantly reduces the file size enabling a detailed analysis locally.

3.2 Particle Identification

To successfully identify the final state particles, information obtained from the (ST), (DC), and Time of Flight (SC) detector must be employed. The SC provides us with the time of travel of the particle from the event vertex to the TOF detector. Since the distance traveled by the particle in the DC is determined by the reconstruction, we can calculate the speed of the particle.

A more refined PID than the initial mass selection can be done using the two independent measurements of β: one from TOF and one from DC, along with the assumption about the particle's mass.

We can calculate the particles speed β_c , using the momentum from the DC :

$$\beta = \frac{p}{\sqrt{p^2 + (m^i_{PDG}c^2)^2}} \tag{8}$$

m^i_{PDG} represents the rest mass of the particle with respect to its entry in the Particle Data Group (PDG) tables. We can then calculate the difference between the measured speed β_m from the TOF and the calculated value β_c.

$$\Delta\beta = \beta_c - \beta_m \tag{9}$$

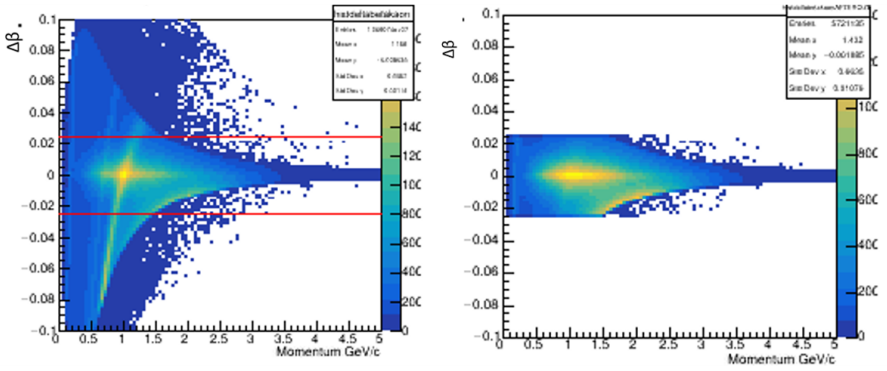

Figure 7: $\Delta\beta$ momentum dependence for the positive K+ track.(Left) before $\Delta\beta$ cuts.(Right) after $\Delta\beta$ cuts.

The DC is also responsible for providing the particle's momentum and charge. Using the momentum we can calculate the mass:

$$m^2 = \frac{p^2(1-\beta_m^2)}{\beta_m^2}, \tag{10}$$

where c = 1.

β_m is the measured velocity, in units of the speed of light, denoted by c.

$\beta_m = \frac{v}{c}$

p is the momentum of the particle.

The calculated mass can be then compared to the already-known masses of particles. The detected particle is therefore identified as the particle with the

best matching mass. To ensure this particle identification and remove background events, we implement cuts on the particle mass ($\Delta\beta$) for the particles of interest (e.g see Fig. 7 for K^+). The example on Fig. 7 presents the $\Delta\beta$ momentum dependence for the positive K^+ track. The left panel shows the distribution before applying $\Delta\beta$ cuts, while the right panel displays the distribution after applying $\Delta\beta$ cuts.

3.3 Photon Selection

The photon that started the reaction is identified by the photon selection cut. This is achieved by contrasting the timing data acquired by the tagger (t_γ) and the CLAS detector (t_{track}). The scattered electrons from the accelerator tunnel go through a magnetic field which bends them into the Tagger when the photons are produced in the tunnel by Bremsstrahlung.

Bremmstrahlung photons are produced by directing electrons onto a gold foil. Subsequently, the electrons are deflected in a dipole magnetic field and detected using a hodoscope. The curvature radius in the dipole depends on the electron's energy, and consequently, the photon energy is determined by the difference in electron energies,

$E_\gamma = E_e - E_{e'}$

The time taken for the photon to reach the event vertex, t_γ is calculated using :

$$t_{gamma} = t_{center} + \frac{d}{c} \tag{11}$$

where d is the distance between the center of the target to the event vertex. CLAS indicates the time at which the reaction starts, whereas tagger information establishes the time at which the photon is absorbed. The difference between the two should be zero for the same photon (see Fig. 8).

$$\Delta t = t_{track} - t_{gamma} \tag{12}$$

3.4 Corrections

3.4.1 Photon Energy Corrections

Due to a small gravitational bulge in the tagger scintillator paddles, photon energy corrections were necessary. The outcome of this gravitational bulge was to reconstruct electrons with systematically higher energies than their true

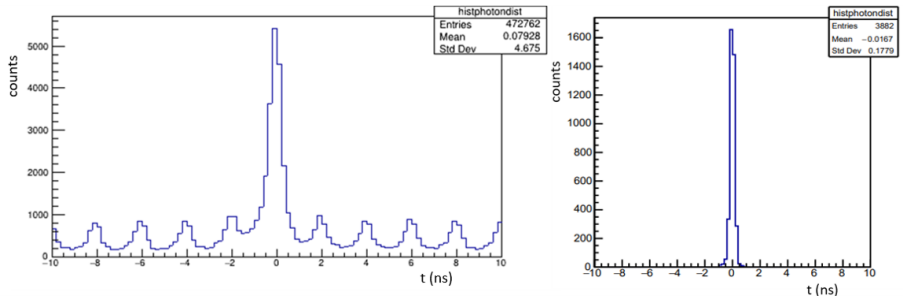

Figure 8: The distribution of the time taken for a photon to reach the event vertex (Left) before cuts and (Right) after cuts.

energies (see Fig. 9). This inaccuracy caused the photon to be tagged with an energy that is lower than its actual energy. In Fig. 10 the energy loss $\Delta E\gamma$ was plotted against the photon energy $E\gamma$. This analysis incorporated the photon energy corrections established by S. Stepanyan et al. [36].

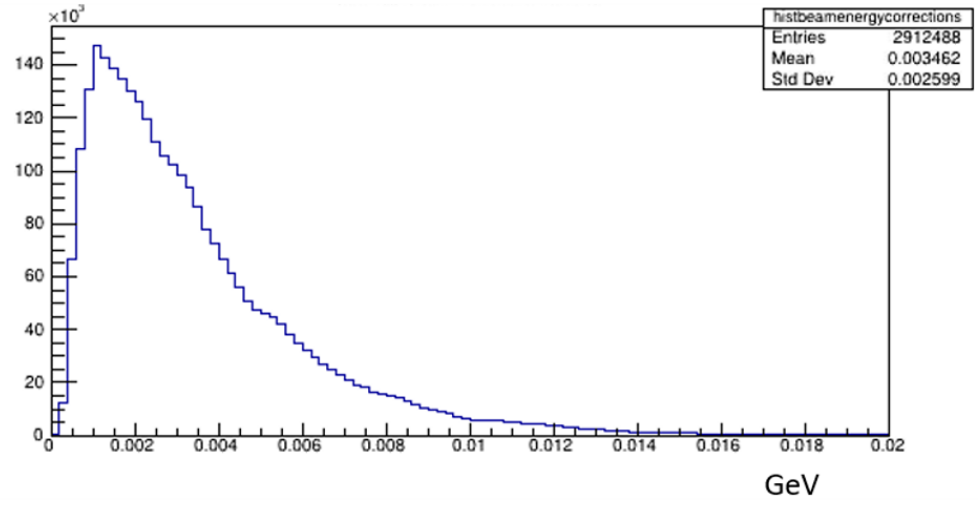

Figure 9: Photon energy spectrum after corrections.

3.4.2 Energy-loss Corrections

Some energy is always lost when charged particles pass through matter, through the ionization or excitation of electrons in the matter. The mean rate of energy loss is given by the Bethe-Bloch equation,

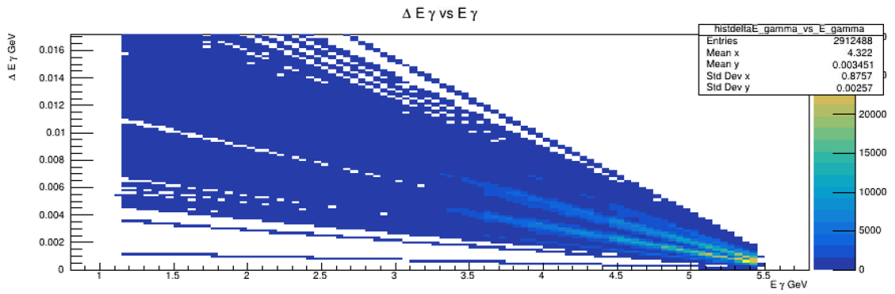

Figure 10: Energy loss as a function of measured photon energy.

$$-\frac{dE}{dx} = Kz^2\frac{Z}{A}\frac{1}{\beta^2}\left(\frac{1}{1}\ln\frac{2m_ec^2\beta^2\gamma^2T_{max}}{I^2} - \beta^2 - \frac{\delta(\beta\gamma)}{2}\right), \tag{13}$$

where A is the atomic mass of the target, Z is the atomic number of the target, I is the mean excitation energy, T_{max} is the maximum kinetic energy that can be gained by an electron in a single collision, and K is a constant that depends on the classical electron radius, Avogadro's number and the mass of the electron.

The energy lost due to ionisation of the target, is corrected using the eloss software package.

3.4.3 Momentum Corrections

The energy lost in the drift chambers, drift chamber misalignments, and discrepancies between the actual toroidal field and the field map used for track reconstruction, have all been taken into factored in by corrections performed on the particle momenta. The corrections that were incorporated in this project were determined by P. Mattione et al. through the kinematic fitting of the reaction $\gamma + d \rightarrow p + p + \pi^-$ [37].

Kinematic fitting of the reaction γ p $\rightarrow$ p π^- π^+. The difference, Δp_i, between the kinematically and eloss-corrected momenta was used to establish the comparison. The average difference, Δp, between the fitted and eloss-corrected momentum was studied for different particles in every sector of the CLAS detector (see Fig. 11).

The difference Δp was also examined as a function of ϕ to account for drift chamber misalignments and variations in the magnetic field map (see Fig. 12).

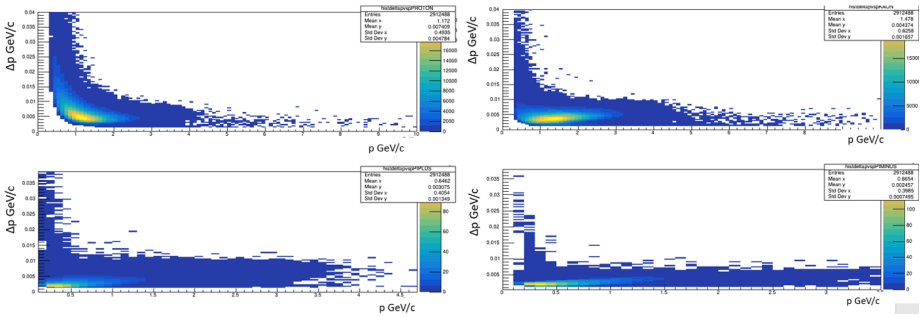

Figure 11: Δp against p for each of the 4 detected particles.(Top Left) proton, (Top Right) Kaon, (Bottom Left) π^+, (Bottom Right) π^-.

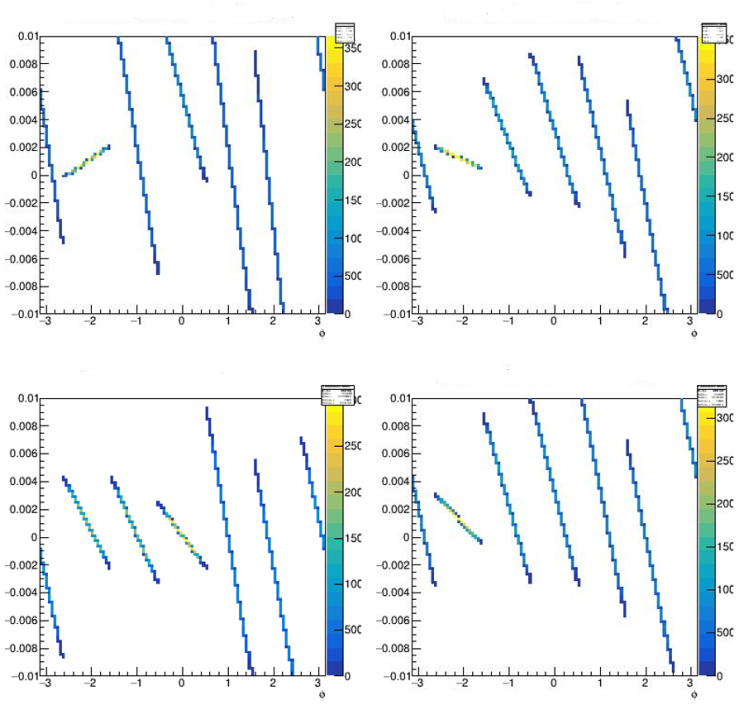

Figure 12: Δp against ϕ for each of the 4 detected particles,(Top Left) Kaon, (Top Right) π^+, (Bottom Left) π^-, (Bottom Right) proton.

3.5 Vertex cut

The vertex is calculated by extrapolating the tracks of the particle determined from the DC, to the position of the target. The distance of closest approach

to the fiducial planes is taken as the vertex position for each track. A more detailed explanation can be found in [38]. Although we expect to find the event vertex inside the target, this is not always true. There exist events that seem to have originated outside target. We therefore opt to perform a vertex cut to remove any events that were not created within the target. From the plot of the vertex position (see Fig. 13) we want to omit any events outside the plateau. The peaks in the plots depict the boundaries of the target.

The coordinate system is set up so that z is oriented in the direction of the photon beam. The negative values on the z axis are due to the fact that the target is placed in the center of the detector.

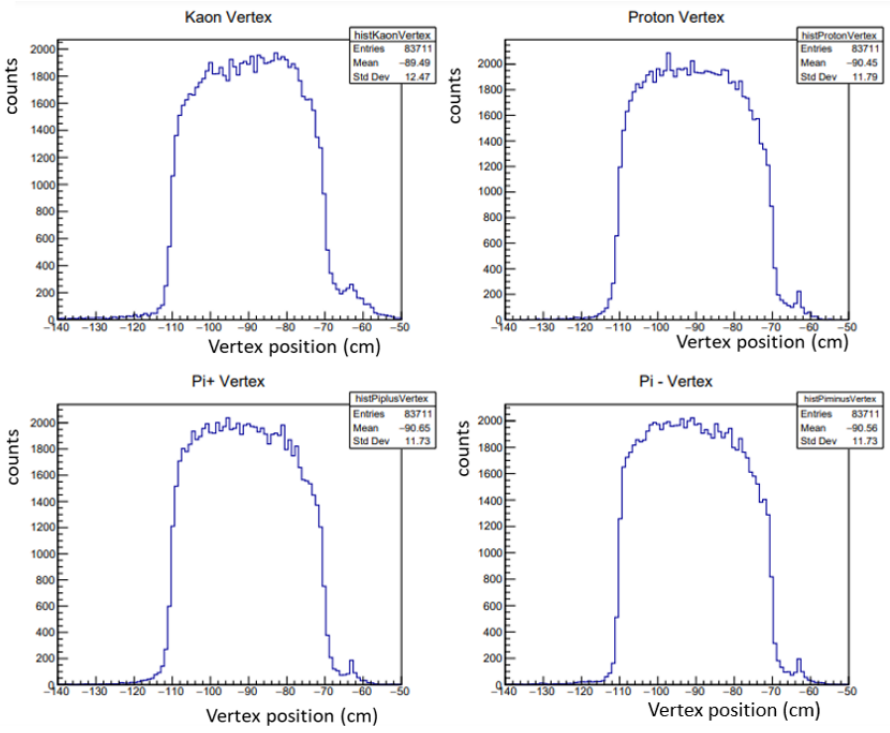

Figure 13: Vertex position (units of cm), parallel to the photon beam) for each of the four detected particles (π^+ ,π^-, K, and proton).

3.6 Reaction Reconstruction

After PID, Photon selection and Vertex cuts were successfully performed on empirical data, there still seemed to exist a need for further analysis. This in

fact rises from the vast background events visible in the missing mass plots. To remove these background events we perform cuts on the missing mass plots of identified particles. The missing mass is calculated using energy and momentum conservation and allows us to select the reaction of interest.

As previously stated, four final state particles (π^+ ,π^-, K, and proton) were detected after the photoproduction reaction, γ p $\rightarrow$ K^+ $\Lambda(1405)$.

Considering that K^+, π^+ and π^- were already detected, events matching a missing neutron were selected. To select events with a neutron, we made straight cuts around the neutron peak in the MM($\gamma p \rightarrow K^+ + \pi^+ + \pi^- + p + X$).

The missing mass distribution of the reaction $\gamma p \rightarrow K^+ + \pi^+ + \pi^- + p + X$ was determined by,

$$MM(\gamma p \rightarrow K^+\pi^+\pi^- pX) = \sqrt{(P_\gamma + P_p - P_{K^+} - P_{\pi^+} - P_{\pi^-})^2} \qquad (14)$$

where, $P_\gamma, P_p, P_{K^+}, P_{\pi^+}, P_{\pi^-}$ are the four-vector momenta of the photon, the proton target, the Kaon and the two pions.

Before plotting the missing mass distribution of ($\gamma p \rightarrow K^+ + \pi^+ + \pi^- + p + X$), and isolating the neutron peak, cuts must be applied to the Invariant Mass distribution of particles in order to clean our events from as much background contribution as possible.

3.6.1 Λ^0 and K^0 cuts

It is not guaranteed in any way that the detected particles are daughter particles of the $\Lambda(1405)$ decay. There is a 65% probability that Λ^0 decays via the pπ^- channel and a 35% chance that Λ^0 decays via the nπ^0 channel. This can lead to a miss-construction of the reaction as some of the detected particles might not originate from the photoproduction reaction of $\Lambda(1405)$ but from the decay of Λ^0.

The invariant mass distribution is determined using,

$$IM(p\pi^-) = \sqrt{(P_p + P_{\pi^-})^2} \qquad (15)$$

From the plot of the Invariant mass of Λ^0 (IM($p + \pi^-$) (see Fig. 14) we want to omit any events within the peak (Within 3 standard deviations of the mass of Λ^0. This peak is responsible for some of the background events around the neutron peak.

The same procedure was repeated with the Invariant mass distribution (calculated by equation 16) of the neutral Kaon (d $\bar{s}$) (see Fig. 15). There is a

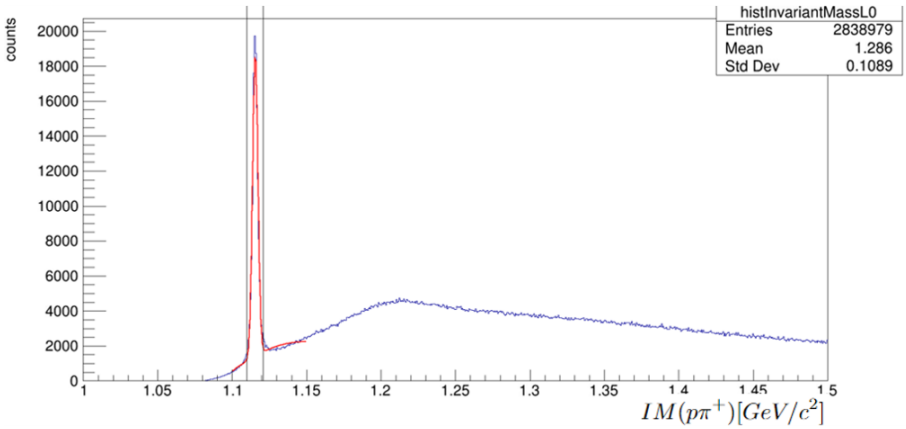

Figure 14: The invariant mass of $p + \pi^-$ showing a clear peak around the Λ mass, which corresponds to background events for our reaction of interest. These events are removed with the application of $\pm 3\sigma$ cuts from the mean of the Gaussian.

69% probability that K^0 decays into two of our final state particles (π^+ and π^-) and it is therefore responsible as well for some of the background events around the neutron peak in the missing mass distribution of $\gamma p \rightarrow K^+ + \pi^+ + \pi^- + p + X$.

$$IM(\pi^-\pi^+) = \sqrt{(P_{\pi^+} + P_{\pi^-})^2} \tag{16}$$

3.6.2 Σ cuts

As it can be seen from Fig. 16 the neutron peak in the MM($K^+\pi^+\pi^-p$) is surrounded by a large peak close to the mass of Σ^-. Since there was no significant visible difference in the MM($K^+\pi^+\pi^-p$) plot after the Λ^0 and K^0 Invariant mass cuts were applied (see Fig. 17), we proceeded to cut incident Σ^- beam and the Σ^- re-scattered events that might be responsible for the background peak.

In order to isolate the peak of neutron missing mass around 939.65 MeV, the next step was to remove the Σ^- beam events outside 3 standard deviations from the mass of Σ^- (1130 and 1270 MeV). For the re-scattered Σ^-, the exact same method was repeated. From (see Fig. 18) it can be seen that after the events that contain a Σ^- particle are eliminated a peak very close to the theoretical mass of the neutron is visible.

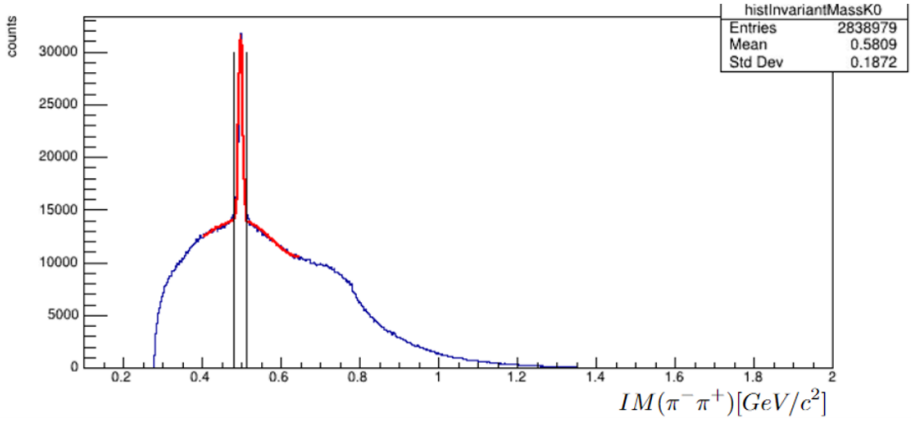

Figure 15: The invariant mass of $\pi^+ + \pi^-$ showing a clear peak around the K^0 mass, which corresponds to background events for our reaction of interest. These events are removed with the application of $\pm 3\sigma$ cuts from the mean of the Gaussian.

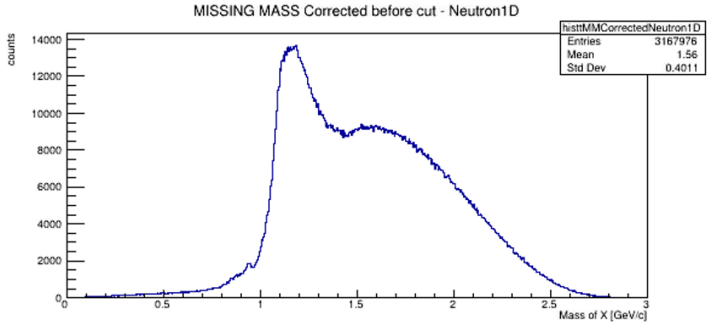

Figure 16: Missing mass of X from the reaction $\gamma p \to K^+\pi^+\pi^- pX$ before cuts.

3.7 Reaction reconstruction and Yield Calculation.

After applying the cuts on the MM described in section 3.6, the reaction characteristics were successfully verified, by removing any events that were possibly detected, which did not originate from the photoproduction of $\Lambda(1405)$. Our next goal was to plot the missing mass plots of the Σ^- and Σ^+ beam (before re-scattering) making it possible to eventually calculate the Yield of Σ^-p and Σ^+p elastic events.

First, the missing mass distribution for the reaction of $\gamma p \to K^+\pi^+ X$ was determined and plotted in order for cuts to be applied and isolate the peak of

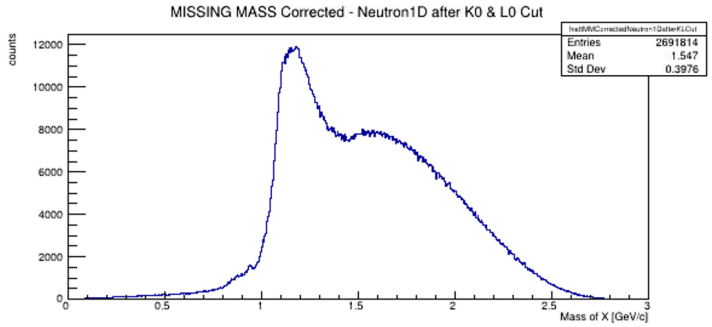

Figure 17: Missing mass of X from the reaction $\gamma p \to K^+\pi^+\pi^- pX$ after Λ^0 and K^0 Invariant mass cuts.

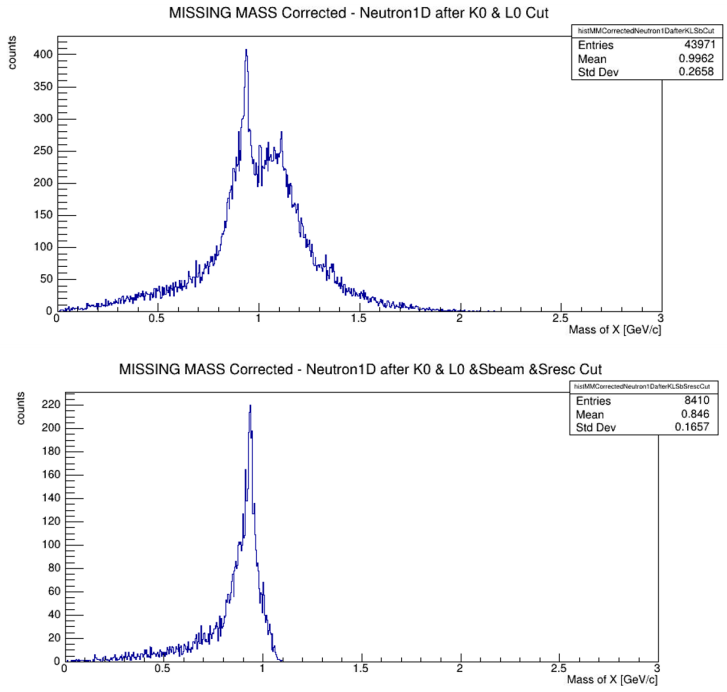

Figure 18: (Top) Missing mass of X from the reaction $\gamma p \to K^+\pi^+\pi^- pX$, after K^0 and Λ^0 and Σ^- beam cut at 1.13 and 1.27 GeV, (Bottom) Missing Mass of X from the reaction $\gamma p \to K^+\pi^+\pi^- pX$, after K^0 and Λ^0, Σ^- beam and Σ^- re-scattered cuts at 1.13 and 1.27 GeV .

Σ^-.

$$MM(\gamma p \to K^+\pi^+X) = \sqrt{(P_\gamma + P_p - P_{K^+} - P_{\pi^+})^2} \tag{17}$$

The missing mass distribution for the Σ^+ peak was determined by,

$$MM(\gamma p \to K^+\pi^-X) = \sqrt{(P_\gamma + P_p - P_{K^+} - P_{\pi^-})^2} \tag{18}$$

Σ^- particle after the photon and vertex selection cuts were applied (see Fig. 19a). Then, just as in previous steps, we implemented the same invariant mass cuts for Λ^0 and K^0 (see Fig. 19b). Subsequently, a criteria was used to ensure the neutron mass to fall between 0.8 and 1.0 GeV so that events containing a neutron would be included(see Fig. 19c). The next stage was to exclude any Σ^- that were more than three standard deviations out from the mass range of Σ^- (1130 to 1270 MeV)(see Fig. 19d).

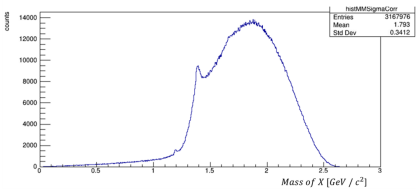

(a) MM($\gamma p \to K^+\pi^+X$) distribution after Vertex, and photon selection cuts.

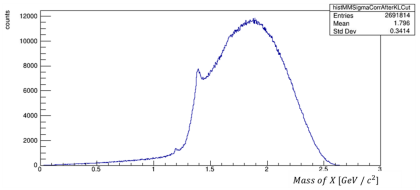

(b) MM($\gamma p \to K^+\pi^+X$) distribution after Vertex, photon selection, Λ and K^0 Invariant mass cuts.

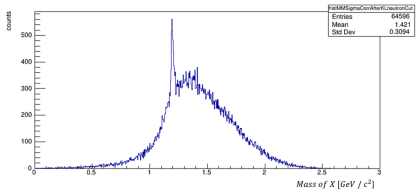

(c) MM($\gamma p \to K^+\pi^+X$) distribution after Vertex, photon selection, Λ and K^0 Invariant mass, neutron cuts.

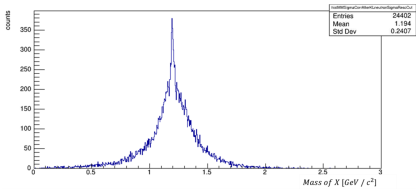

(d) MM($\gamma p \to K^+\pi^+X$) distribution after Vertex, photon selection, Λ and K^0 Invariant mass, neutron cuts and $\Sigma-$ re-scattered cuts.

Figure 19: Grid of Plots of the reaction of $MM(\gamma p \to K^+\pi^+X)$ that reconstructs the missing mass of the Σ^- beam.

The plot 19d was utilised in determining the Yield of the scattering reaction, which was then used in the determination of the cross section ratios of the

reactions.

4 Cross Section determination

This section outlines the steps that were necessary for the determination of the cross section of the Σp scattering reactions.

The cross section quantifies the probability for a specific reaction to occur. The magnitude of the cross section of the Σ^- scattering is analogous to the strength of the interaction between the Σ^- hyperon and the proton nucleon. The same is true for the interaction of $\Sigma^+ p \to \Sigma^+ p$.

For the purpose of enhancing the readability in the subsequent derivations, Σ was used to represent both Σ^+ and Σ^- baryons, given that the equations are identical for both.

The cross section of the reaction is given by:

$$\sigma = \frac{N_\Sigma}{L_\Sigma \cdot A} \tag{19}$$

where A is the acceptance of the detector discussed in 4.2 and N_Σ is the number of Σp elastic collision events determined in 4.4 and L_Σ is the photon beam luminosity discussed below.

4.1 Luminosity

In particle physics, Luminosity is the term given to the quantity that measures the number of interactions that can be produced in an experiment.

The luminosity of Σ^- or Σ^+ beam from eq. 19 can be determined by eq. 20.

$$L_\Sigma = \frac{N_A \cdot \rho_T \cdot l_\Sigma \cdot N_\Sigma}{M} \tag{20}$$

where, N_A is the Avogadro number,

ρ_T is the density of the target,

M is the molar mass of the target.

l_Σ is the path length of the Σ particles within the target cell,

and N_Σ is the number of Σ events which is identical to the number of $\Lambda(1405)$ particles. This is due to the fact that because of the very short lifetime of $\Lambda(1405)$, all of them will decay into Σ baryons.

The number of $\Lambda(1405)$ particles can be found using the well-known cross-sections of the $\Lambda(1405)$ the acceptance(see 4.2) and the luminosity of the photon beam.

The luminosity of the photon beam is defined by,

$$L_\gamma = \frac{N_A \cdot \rho_T \cdot l_T \cdot N_\gamma}{M} \tag{21}$$

where, N_A is the Avogadro number, ρ_T is the density of the target, l_T is the path length, N_γ is the photon beam flux, and M is the molar mass of the target.

The utilization of luminosity in the cross section calculations necessitates knowledge of the photon beam flux and the path length.The process of obtaining the path lengths of the Σ^+ and Σ^- is a complex process that demands additional time resources. Unfortunately, given the time constraints of this one-year project, dedicating the requisite time to acquire the experimental path lengths was deemed impractical. See subsection 4.5.1 for more detailed explanation on the limitations of obtaining experimental path lengths.

4.2 Acceptance

The determination of the cross section of the Σ^- beam requires the knowledge on the acceptance of the detector. A detailed analysis would be necessary to obtain an in-depth knowledge of the detector acceptance for cross section measurements. However, by determining the cross section ratio of the $\Sigma+$ to the Σ^- beam we only need to demonstrate that the detector acceptance is the same for the two elastic re-scattering reactions. To show this the momentum distribution of Σ^+ and Σ^- was plotted after applying minimum momentum and angle θ (in rad) cuts on the the final state particles of the reaction (see Fig. 21).

From the following plot of the momentum distributions of Σ^+ and Σ^- we can see that the two particles have the same momentum distribution, and therefore we can conclude that the detector in both reactions must have the same acceptance or this would not be possible.

4.3 Cross Section ratio

Moreover, the use of cross section ratio alleviates from the photon beam flux determination through the following derivation :

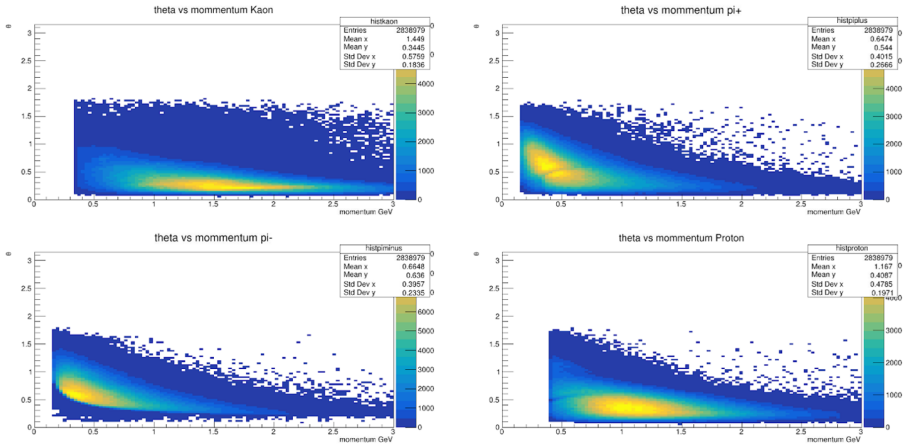

Figure 20: Plots of Particle cuts.(Top left) Kaon + : momentum > 0.35 GeV/c and $\theta > 0.05$ rad. (Top right) π^+ : momentum > 0.15 GeV/c and $\theta > 0.05$ rad.(Bottom left) π^-: momentum > 0.15 GeV/c and $\theta > 0.05$ rad. (Bottom right) proton momentum > 0.40 GeV/c and $\theta > 0.05$ rad.

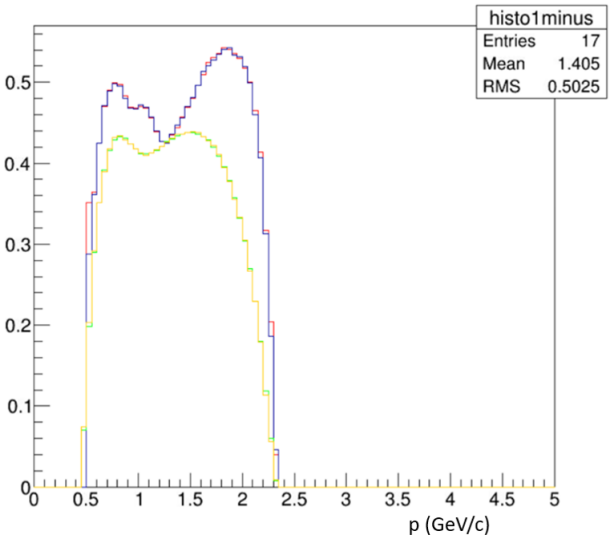

Figure 21: Momentum distribution of Σ^+ and Σ^- after K, π^-, proton, and π^+ cut. (Blue line) Σ^+, (Red line) Σ^-, (Green line) Σ^+ without the Legendre cross sections, (Orange line) Σ^+ without the Legendre cross sections.

$$\frac{\sigma_{\Sigma^+}}{\sigma_{\Sigma^-}} = \frac{\frac{N_{\Sigma^+}}{L_{\Sigma^+} \cdot A}}{\frac{N_{\Sigma^-}}{L_{\Sigma^-} \cdot A}} \tag{22}$$

If the acceptance of the detector is on average the same for the two reactions, then the cross section ratio simplifies to:

$$\frac{\sigma_{\Sigma^+}}{\sigma_{\Sigma^-}} = \frac{N_{\Sigma^+} \cdot L_{\Sigma^-}}{N_{\Sigma^-} \cdot L_{\Sigma^+}} \tag{23}$$

And since the target and setup is the same for both decay channels of $\Lambda(1405)$ (Σ^- and Σ^+) then the ratio of the luminosities of the two Σ particle simplifies to the ratio of their corresponding path lengths. The cross section ratio eventually reduces to a ratio of the Yields of the two reactions and the inverse of the ratio of the path lengths:

$$\frac{L_{\Sigma^-}}{L_{\Sigma^+}} = \frac{\frac{N_A \cdot \rho_T \cdot l_{T_{\Sigma^-}} \cdot N_\gamma}{M}}{\frac{N_A \cdot \rho_T \cdot l_{T_{\Sigma^+}} \cdot N_\gamma}{M}} = \frac{l_{T_{\Sigma^-}}}{l_{T_{\Sigma^+}}} \tag{24}$$

$$\frac{\sigma_{\Sigma^+}}{\sigma_{\Sigma^-}} = \frac{N_{\Sigma^+} \cdot l_{\Sigma^-}}{N_{\Sigma^-} \cdot l_{\Sigma^+}} \tag{25}$$

Although both Σ particles have very short lifetimes and will decay before they reach the detector. However, their lifetimes and hence the distance that they will travel before decaying is different. The path length can be given by the following equation, $l = ct$ where c is the speed of light and t is the lifetime of each particle ($t_{\Sigma^-} = 1.479 \times 10^{-10}\,\text{s}$ and $t_{\Sigma^-} = 0.8018 \times 10^{-10}\,\text{s}$) .

4.4 Yield determination

The missing mass distribution's peak can be fitted using a Gaussian Probability Density Function (PDF) due to the fact that, after the several cuts that were applied the signal events cluster around the mass of the Σ baryon. This characteristic of the missing mass distribution aligns with the shape of a normal distribution. It can be therefore concluded that it can be fitted with some degree of uncertainty with a Gaussian PDF.

The background signal exhibits a smooth variation across the range of missing mass distribution. A Polynomial PDF, has the ability to interpolate between the missing mass data points, providing a continuous representation of the background distribution.

To calculate the Yield of $\Sigma^{\pm}$ the reaction $\gamma p \to K^{+}\pi^{\pm}X$ was plotted. The number of events from the missing mass plot of $\Sigma^{\pm}$ was calculated by subtracting the polynomial of the fit from the Gaussian of the peak and Fig. 23 for a range of momentum bins. As an example the missing mass plot for the momentum bin of 0.9 - 1.0 GeV/c, for both the Σ^{-} (see Fig. 22) and Σ^{+} (see Fig. 23). More missing mass distributions for both Σ particles, were taken for a range of different momentum bins(see Appendix A).

$$f(x) = A \cdot e^{-\frac{(x-\mu)^2}{2\sigma^2}} + Bx + Cx^2 + Dx^3 + \dots \tag{26}$$

Here:

$f(x)$ is the overall function representing the $\Sigma^{\pm}$ missing mass distribution,

A is the amplitude of the Gaussian peak,

μ is the mean of the Gaussian peak,

σ is the standard deviation of the Gaussian peak,

$B, C, D, \dots$ are coefficients of the polynomial background terms,

x is the variable representing the $\Sigma^{\pm}$ mass.

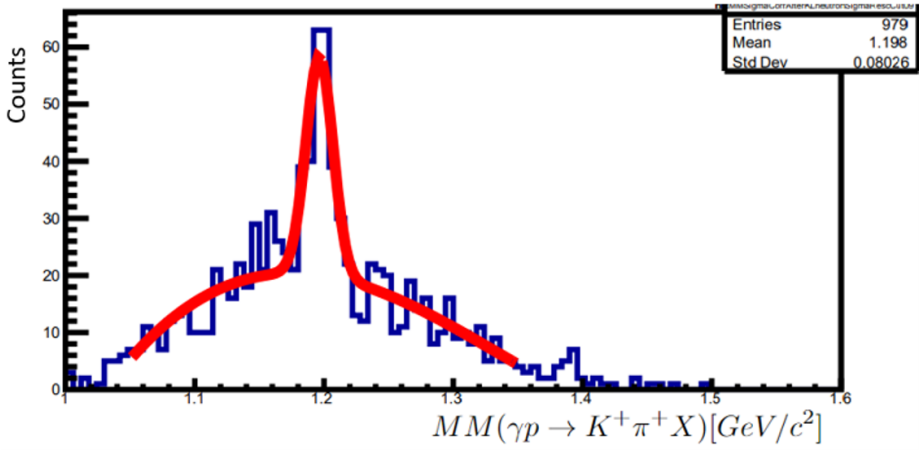

Figure 22: $MM(\gamma p \to K^{+}\pi^{+}X)$ distribution where the peak matches the mass of Σ^{-} in GeV/c^2, for the momentum bin of 0.9 - 1.0 GeV/c.

The Yield is therefore given by,

$$N_{\Sigma^{+}} = \frac{\int_{\text{gaussian}} d(M_{\Sigma^{+}}) - \int_{\text{polynomial}} d(M_{\Sigma^{+}})}{\text{binwidth}} \cdot \frac{1}{0.4831} \tag{27}$$

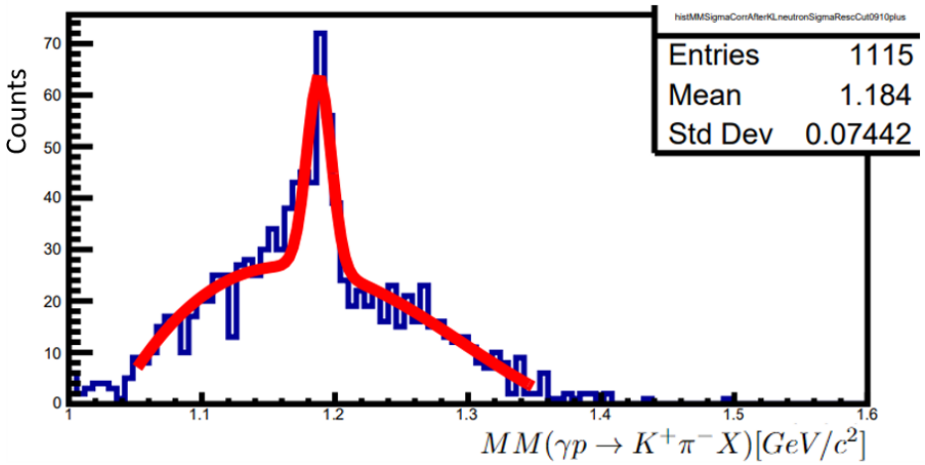

Figure 23: $MM(\gamma p \to K^+\pi^- X)$ distribution where the peak matches the mass of Σ^+ in GeV/c^2, for the momentum bin of 0.9 - 1.0 GeV/c.

$$N_{\Sigma^-} = \frac{\int_{\text{gaussian}} d(M_{\Sigma^-}) - \int_{\text{polynomial}} d(M_{\Sigma^-})}{\text{binwidth}} \tag{28}$$

Where 0.4831 is the probability that the Σ^+ particle will decay via the $\Sigma^+ \to n\pi+$ channel into the detected final state particles. For Σ^- the probability that the Σ^- particle decays into a neutron and a π^- is equal to 1, and thus there is no need to factor it from the yield N_{Σ^+}.

4.5 Reaction Simulation

The number of proton target particles, N_t, is typically determined by calculating the measured length of the target and multiplying it by appropriate factors such as target density, atomic mass number, and Avogadro's number ($N_A = 6.02 \times 10^{23}$). This provides a straightforward diagnostic for N_t.

However, determining of the number of particles in the $\Sigma-$ beam, is more complicated. Since the Σ particles are secondary particles in this reaction, it is an arduous process to locate the event vertex where the $\Lambda1405$ decay onto the Σ particles. Additionally a direct beam diagnostic is not available to count the number of $\Lambda1405$ particles that are photoproduced.

Moreover, the beam Σ is generated within the target, rendering any protons upstream of the Σ production vertex unavailable for subsequent Σp elastic scattering. $\Sigma-$ has a decay path of 4.43 cm while $\Sigma+$ of 2.40 cm which are much

smaller than the 40 cm target length. In addition to that, the Σ particle quickly decays, making proton targets downstream of the Σ decay vertex unavailable for later scattering. Furthermore, unlike the photon beam produced by the accelerator, the Σ beam does not travel parallel to the target axis and can exit the target through the cylindrical wall long before travelling the entire target length. The complex nature of Σ production and decay requires more sophisticated methods for estimating the decay path of Σ particles in the experimental setup.

As a solution for the aforementioned limitations of obtaining the experimental path lengths, a simulation of the reaction was used to obtain the path lengths needed for the cross section ratio calculations.

4.5.1 Simulation characteristics

The simulation was constructed by writing a C++ code that served as a generator for the reaction $\gamma p \to K\Lambda(1405)$, followed by the decays $\Lambda(1405) \to \Sigma^-\pi^+$ and the elastic re-scattering $\Sigma^- p \to \Sigma^- p$ or $\Lambda(1405) \to \Sigma^+\pi^-$ and the elastic re-scattering $\Sigma^+ p \to \Sigma^+ p$.

The simulation is based on the generation of events based on random numbers and kinematic calculations used to model the particle interactions that follow the decay of $\Lambda(1405)$. A Monte Carlo phase space generator was used to generate events with intended decay branching ratios. For a more detailed description of the simulation generator please [39].

Legendre polynomials are used to model the differential cross-section as a function of energy and scattering angle, which are then incorporated in the simulation, to compute the particle paths within the target.

$$P_n(x) = \frac{1}{2^n n!}\frac{d^n}{dx^n}(x^2-1)^n \tag{29}$$

$$\sigma(\cos\theta) = C_0 + C_1 P_1(\cos\theta) + C_2 P_2(\cos\theta) + C_3 P_3(\cos\theta) + C_4 P_4(\cos\theta) \tag{30}$$

Subsequently the generator includes the tertiary decay of Σ^- into the final state particles $n\pi^-$.

4.5.2 Σ Decay Path Length determination

Path length determination within target cell (formula we use to calculate the path length depending on the Sigma momentum, and direction) Path length

results for each Sigma accounting for their different lifetimes.

The simulation code generates $\Lambda 1405$ particles and then decays them into $\Sigma^{\pm}$ particles. The $\Sigma^{\pm}$ production vertices are uniformly distributed throughout the target. The production vertex and the target geometry are used to determine the hyperon's path length as it travels through the target before decaying. However, to derive the path length we must first calculate the longitudinal path and exit z coordinate.

During this simulation of events we shall see that a series of assumptions have been made. The first assumption was that the cylindrical target cell is oriented along the z-axis with its center located at (0,0,$l_T/2$ where l_T is the length of the target cell, in this case 40 cm. The vertex coordinates, x0 and y0, are generated randomly and uniformly on a disc whose radius is equal to that of the cylinder, i.e 2 cm. Using uniformly distributed random values between 0 and 2π, the azimuthal angle ϕ_V of the vertex measured from the positive x-axis, can be determined.

The distance of the vertex from the centre is given by,

$$r_0 = \sqrt{\text{Rnd}} \times r \tag{31}$$

Where Rnd is a random number and r is the radius of the cylindrical target cell.

The distance is taken uniformly along the z-axis between 0 and 40 cm. The vertex position is calculated using,

$$x_0 = r_0 \times \cos(\phi_V) \tag{32}$$

$$y_0 = r_0 \times \sin(\phi_V) \tag{33}$$

$$z_0 = z_0 \tag{34}$$

Through the geometry of the cross section of the cylindrical target, the path length Σ^- particle travelling at an angle ϕ_p can be determined (see Fig. 25).

From the cosine rule,

$$r^2 = r_0^2 + l^2 + 2r_0 l\cos(\pi - \phi_p + \phi_v) = r_0^2 + l^2 + 2r_0 l\cos(\pi - (\phi_p - \phi_v)) \tag{35}$$

Using the identity,

$$\cos(\pi - x) = -\cos(x) \tag{36}$$

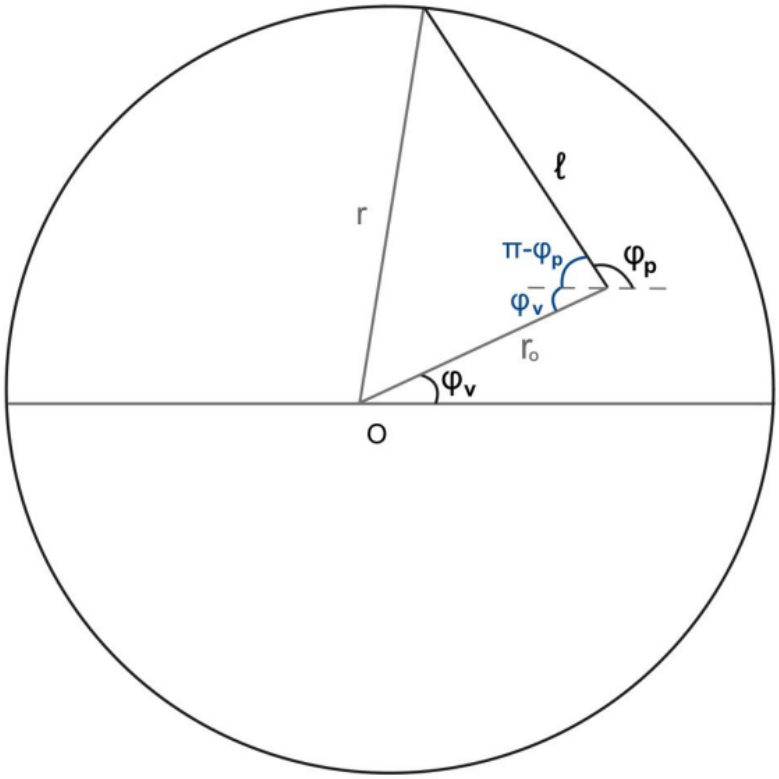

Figure 24: Cross section of the path of $\Sigma^{\pm}$ in the cylindrical target cell.

$$r^2 = r_0^2 + l^2 - 2r_0 l\cos(\phi_p - \phi_v) \tag{37}$$

if we rearrange it into the quadratic form we get :

$$l^2 + [2r_0\cos(\phi_p - \phi_v)]l + r_0^2 - r^2 = 0 \tag{38}$$

Solving with the quadratic formula we can finally get the path in the xy plane,

$$l = -r_0\cos(\phi_p - \phi_v) \pm \sqrt{r_0^2\cos^2(\phi_p - \phi_v) + r^2 - r_0^2} \tag{39}$$

The longitudinal path is therefore given by,

$$l_l = \frac{l}{\tan(\theta)} \tag{40}$$

and the exit z-coordinate is calculated as,

$$z_{exit} = l_l + z_0 \tag{41}$$

For z_{exit} between 0 and l_T, the length of the target, the path is calculated by,

$$Path = l/\sin\theta \tag{42}$$

The Σ^- particle can exit through the target ends if z_{exit} is larger than the target cell length, that is, $z_{\text{exit}} < 0$ or $z_{\text{exit}} > l_T$. This is particularly true if it was created near the target's ends or at a small angle. The path length is calculated as follows,

$$\text{Path} = \begin{cases} \frac{l_T - z_0}{\cos(\theta)}, & \theta < 90^\circ \\ \frac{z_v}{\cos(\theta)}, & \theta > 90^\circ \end{cases}$$

where z_v is the z-coordinate of the event vertex.

From the following plot, we can see that the $\Sigma-$ particles are created at small angles ($\theta > 90^\circ$), and thus the first solution must be employed.

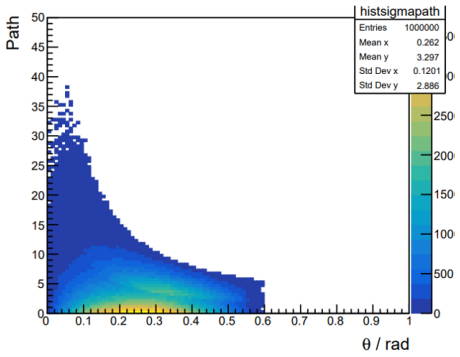

Figure 25: Path of the hyperon against scatering angle θ of Σ^- .

As previously mentioned, $\Sigma-$ has a decay path, ct, of 4.43 cm while $\Sigma+$ of 2.40 cm which are much smaller than the 40 cm target length. Therefore, a high probability exists, that the $\Sigma^{\pm}$ particle decays prior to exiting the target or interacting with a proton. To account for this the path length must be weighted by the probability of decaying, which is given by,

$$P(d) = \exp\left(-\frac{d}{\beta\gamma c\tau}\right) \tag{43}$$

where $\beta = v/c$ and γ is the Lorentz boost.

The path length at last is calculated using :

$$Path = \beta\gamma c\tau \tag{44}$$

4.5.3 Path Length results

The Path was taken from the generator code by plotting the 2-dimensional histogram of Path against the Σ^- beam momentum , for the same momentum bins that the yield was calculated (0.6 - 1.8 GeV/c). The result was projected as a 1D histogram from which the mean path length was extracted(see Fig. 26). The same procedure was repeated for the Σ^+ beam after changing the mass and lifetime in the code.

The 1D histogram for both Σ baryons is shown below for the momentum bin 0.9-1.0 GeV/c.The same procedure was repeated for the Σ^+ beam after changing the mass and lifetime in the code (see Fig. 27). See Appendix A for the plots of the path length of Σ^- and Σ^+ for all the momentum intervals used in this analysis.

5 Results

5.1 Cross section ratio as a function of Momentum

The ultimate goal of this analysis was to determine the cross-section ratio of the $\Sigma^- p \to \Sigma^-$ elastic scattering reaction with the anticipation that it would provide some inside to the Σ^+ and Σ^- hyperon-nucleon interactions. The cross section ratio was determined as a function of the momentum of the hyperon (Σ) beam. A thorough analysis on how this was done can be found on section 4.

We would normally expect that the cross section σ, of Σ^+, would be larger than the σ of Σ^-. This is due to the fact that there is a higher probability that Λ1405 decays into a Σ^+ rather than a Σ^- particle.

From figure 28 it can be observed that the cross section ratio is significantly higher in the momentum range of 0.6-0.7 GeV/c.This likely influenced by the considerably smaller yield for both Σ particles and especially for the Σ^-. The presence of particles with momenta less than 0.7 GeV/c is notably scarce, and this is also apparent when examining the momentum distribution of $\Sigma^+ p$ and Σ^- in figure 29. The low yields at lower momenta have larger statistical fluctu-

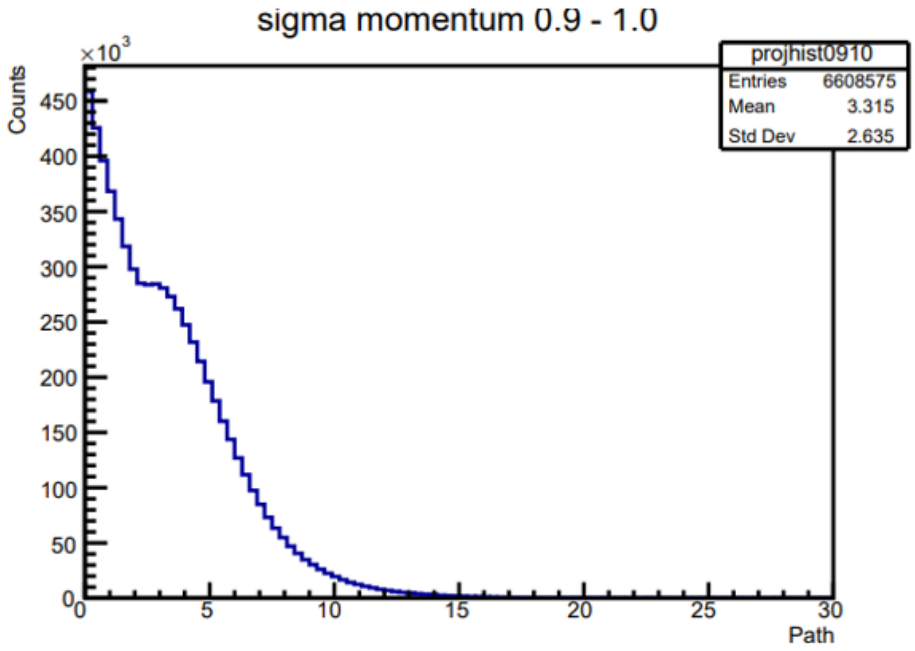

Figure 26: Path length distirbution of Σ^- in GeV/c, at the momentum interval 0.9 - 1.0 GeV/c.

ations and more importantly there will be a larger uncertainty in determining background contributions, making it very difficult for the polynomial probability density function to fit.

Furthermore, it can be observed that a small "dip" is present. The error in the cross section ratio (see 5.3 for details on how they were calculated) is not large enough to account for this decrease in the ratio around 1 GeV/c.

To get a clearer picture, we collected more cross-section ratio values with smaller bins around the dip. This way, we could pinpoint exactly where the dip occurs in terms of momentum (see figure 30). We took more $\frac{\sigma^+}{\sigma^-}$ values at momentum bins of 1 GeV/c. The error in the σ ratio increased as the momentum bins became smaller, but not enough to account for the dip in the cross section ratio.

5.2 Cross section ratio as a function of Energy

Plotting the cross-section ratio against the total energy of the reaction W, can offer a comprehensive understanding of the energy dependence of this elastic

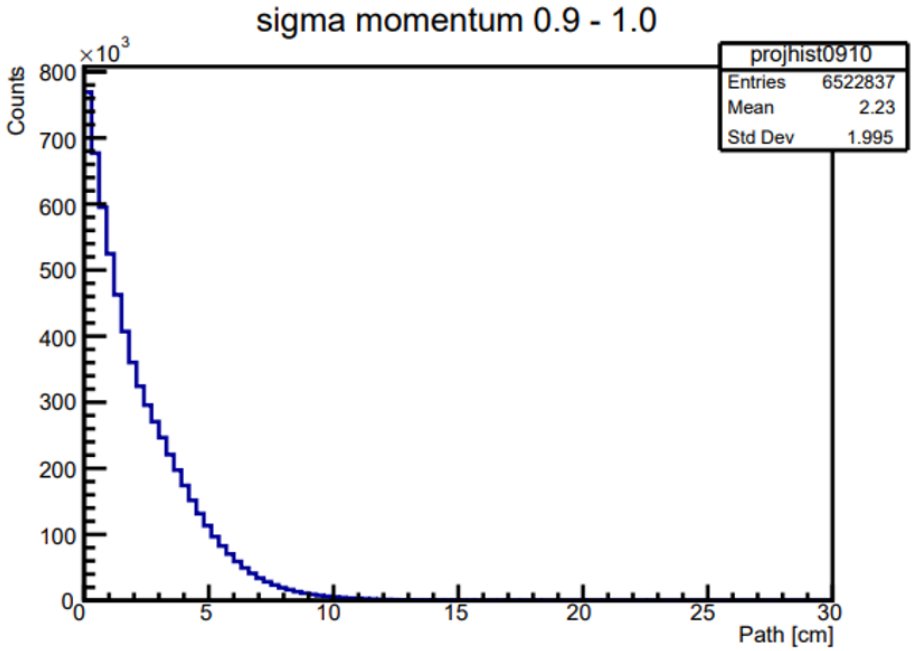

Figure 27: Path length distribution of Σ^+ in GeV/c, at the momentum interval 0.9 - 1.0 GeV/c.

scattering. It allows for comparisons with the Cross Section ratio of $\frac{\Sigma^+}{\Sigma^-}$ against momentum plots, which may help to provide additional understanding in the physics of the $\Sigma^- p \to \Sigma^- p$ interaction.

From figure 31, we can see that the two plots are identical in shape. Since the $\Sigma^- p$ interaction is an elastic collision, both energy and momentum are conserved. It was therefore expected to see the same shape in the two plots as any difference would indicate that some energy was not conserved. In this analysis, W was derived using the momentum of the Σ^- beam,

$$W = \sqrt{M_\Sigma^2 + M_p^2 + 2 \cdot (M_p \times \sqrt{M_\Sigma^2 + P_\Sigma^2})} \tag{45}$$

where M_Σ is the rest mass of Σ, M_p is the rest mass of the proton, P_Σ is the momentum of the Σ beam and the term $2 \cdot (M_p \times \sqrt{M_\Sigma^2 + P_\Sigma^2})$ is the Kinetic Energy of the Σ beam.

Furthermore, contrast between the two plots, could have been a result of a systematic error, caused by a malfunction in the detector system that measures

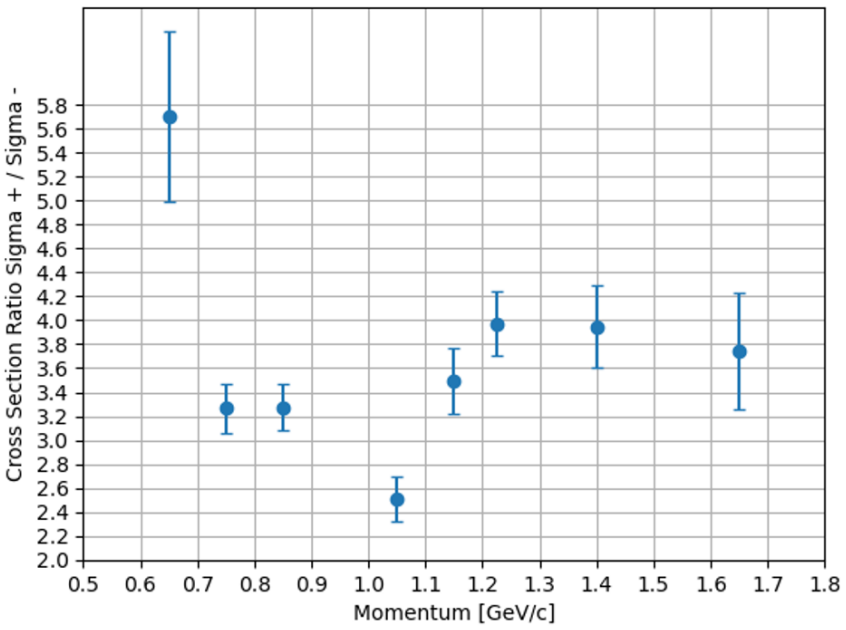

Figure 28: Cross Section ratio of $\frac{\Sigma^+}{\Sigma^-}$ against momentum in GeV/c, at 8 momentum intervals between 0.6 - 1.8 GeV/c.

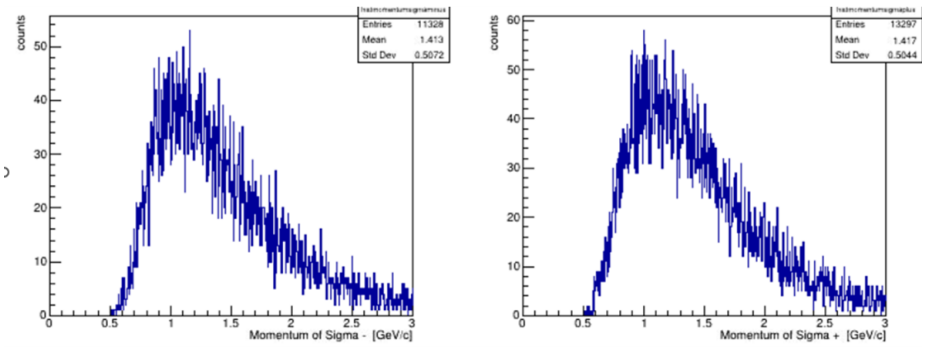

Figure 29: Momentum distribution of Σ^+ and Σ^- particles in GeV/c, at between 0.5 - 3.0 GeV/c.

the momentum.

The appearance of the dip in both plots indicates that further investigation is required to unravel its nature.

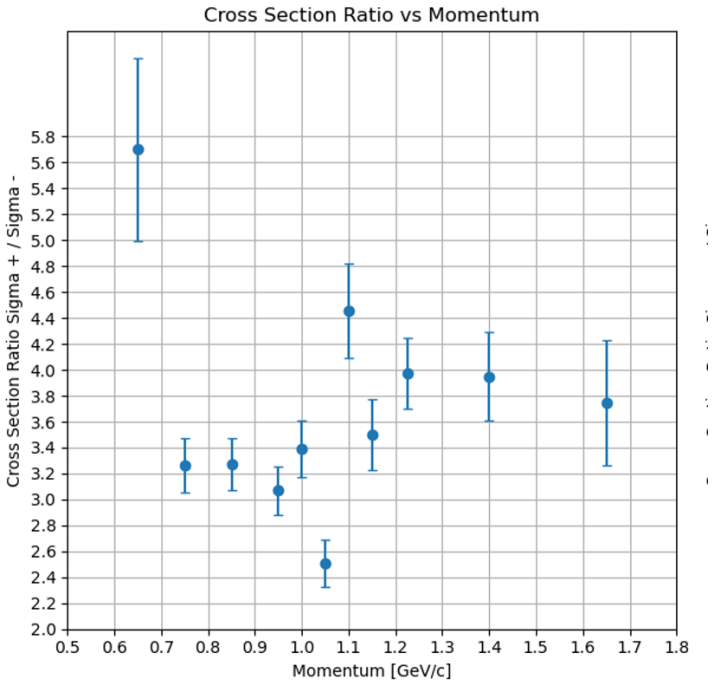

Figure 30: Cross Section ratio of $\frac{\Sigma^+}{\Sigma^-}$ against momentum in GeV/c, at 10 momentum intervals between 0.6 - 1.8 GeV/c.

5.3 Errors

Since we are only concerned with the ratio of the cross sections, the error of the path length obtained from the simulation can be neglected as this is the same for both the Σ^+ and Σ^-. As the Yield was obtained experimentally the error in these values must be taken into account.

The error in the Yield is determined by fist calculating the integral error within 3σ from the mean of the momentum distribution. The error in the Yield is then given by,

$$E_{N_{\Sigma^+}} = \sqrt{N_{\Sigma^+} + (E_{Integral_{\Sigma^+}} \times E_{Integral_{\Sigma^+}})}. \tag{46}$$

The error in the Yield can be then used to find the error in the σ-ratio. This was determined as the propagation of uncertainty using the standard deviation formula of the function f. Function f can be understood as the value of the function determined from the expectation value of A and B . In this case the

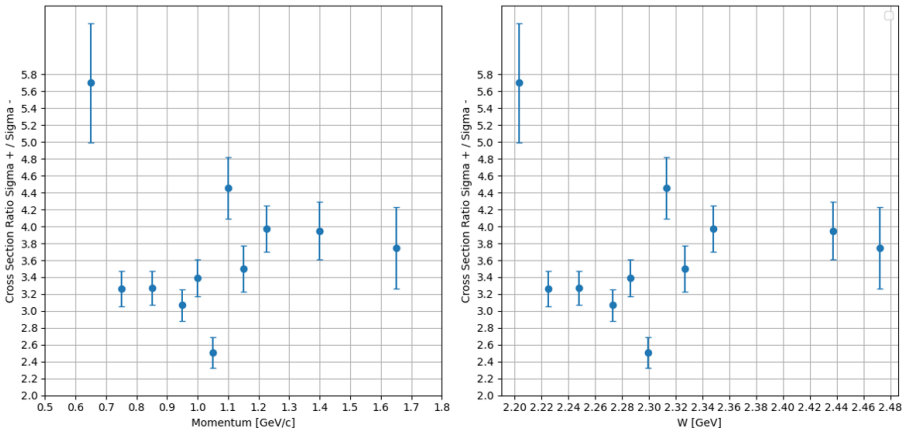

Figure 31: (Left) Cross Section ratio of $\frac{\Sigma^+}{\Sigma^-}$ against momentum in GeV/c, at 10 momentum intervals between 0.6 - 1.8 GeV/c. (Right) Cross Section ratio of $\frac{\Sigma^+}{\Sigma^-}$ against W in GeV, at 6 energy intervals between 2.2 and 2.5 GeV.

function f is the ratio of $\frac{\Sigma^+}{\Sigma^-}$.

$$f = \frac{A}{B} \tag{47}$$

where A is the yield of Σ^+ and B is the yield of Σ^-.

$$\sigma_f = f \cdot \sqrt{\left(\frac{\sigma_A}{A}\right)^2 + \left(\frac{\sigma_B}{B}\right)^2} \tag{48}$$

Which in terms of the ratio becomes,

$$E_{\text{Ratio}} = \frac{N_{\Sigma^+}}{N_{\Sigma^-}} \cdot \sqrt{\left(\frac{E_{N_{\Sigma^-}}}{N_{\Sigma^-}}\right)^2 + \left(\frac{E_{N_{\Sigma^+}}}{N_{\Sigma^+}}\right)^2} \tag{49}$$

The error in the ratio was then plotted as vertical error bars in the plots against momentum and energy.

6 Discussion

The presented analysis was concerned with the preliminary results of the cross section ratio of the two Σp scattering reactions. Further studies on the systematic uncertainties must be carried out to allow for a better understanding of this particular hyperon-nucleon interaction. Furthermore, more detailed simulations are imperative to unravel the intricacies of the detector acceptance. The use

of GSIM, the official Geant Simulation framework of CLAS is the natural next step for the determination of the acceptance. A more detailed explanation on the GSIM can be found on the JLab website. [40].

Although this analysis was concerned with obtaining the experimental cross section ratio of the Σ particles, the reactions were further studied theoretically in order to make comparisons with the experimental results.

6.1 Cross Section Ratio from Clebsch-Gordon Coefficients

For the theoretical determination of the cross section ratio we employed the use of the Clebsch-Gordon coefficients, from the work of Tadasha Dash & Anjana Acharya [41]. However, before introducing the Clebsch-Gordon coefficients we should first introduce the Isospin.

6.1.1 Isospin

Invented by Werner Hisenberg, the Isospin is a quantum number associated with particles that interact via the strong force, i.e Hadrons. It is derived from the flavour symmetry and was created to express the fact that in the eyes of the strong force, there is no difference between a proton and a neutron. The Isospin is conserved in the strong interaction but not in the electromagnetic and weak interaction. Mathematically this means that the Isospin operator commutes with the Hamiltonian of the strong interaction but not of the electromagnetic and weak hamiltonians.

Although the Isospin is not related in any way to the spin, their mathematical properties are identical. This suggests that isospin can be combined the same way that in quantum mechanics angular momentum is added. Particles with the same Isospin number belong to the same the isospin multiplet. This is in a similar fashion that the number of electrons spin states , that are part of the same multiplicity, are given by 2s + 1. In a similar way, the number of states in an isospin multiplet is given by $M = 2I + 1$. i.e. takes values of integers or half integers.

The main difference of the isospin from the spin is that the isospin is unaffected by rotations and therefore is not coupled with the angular momentum of the particle. For this reason, the third component of Isospin I_z(the Isospin in the z-direction), is used to distinguish between particles. I_z takes discrete values from -I to I and it always takes values of multiples of $\frac{1}{2}$.

The different types of Hadrons have different multiplet numbers. For example, since nucleons for example have a 2 allowed states, one being the proton and the other one the neutron, the must have a multiplet of M = 2 and therefore an Isospin of 1/2 (from I =(M – 1)/2 = 1/2). The I_z has to either be equal to $-\frac{1}{2}$ (in the case of the neutron) or $\frac{1}{2}$ (for the proton).

The charge of a state and I_z are related by the Gell-Mann-Nishijima relation [42],

$$Q = I_z + \frac{1}{2}B + \frac{1}{2}S \tag{50}$$

where B is the Baryon number, and S is the strangeness.

6.1.2 Clebsch-Gordon Coefficients

The Clebsch-Gordon coefficients are quantum numbers that are most often used to describe the coupling of two angular momenta, such as the spin and orbital angular momentum of a single particle. In this case, the Clebsch-Gordon coefficients were utilised to describe the coupling of the Isospin with the Isospin projection in the z-direction. The Clebsch-Gordon coefficients are denoted by the symbol $C^{JM}_{J_1M_1,J_2M_2}$, where J_1 and J_2 are the Isospins of the two interacting particles being coupled, M_1 and M_2 are their respective projections onto the z-axis, and J and M are the resulting total Isospin and its projection.

To determine the allowed values of the Clebsch-Gordon coefficients for the Σp interaction, we must first ensure that Isospin is conserved in the interaction. For a reaction to be allowed to occur via the strong interaction Isospin must be conserved (among other things).

The Σ baryon has I = 1 and I_z = -1, 0, 1. From the Gell-Mann-Nishijima equation we can assign each of the I_z to the different states of the particle (Σ^-, Σ^0, Σ^+).The Isospin states are given the notation $|I, I_z\rangle$.

Subsequently, we can verify that both the $\Sigma^- p \to \Sigma^- p$ and $\Sigma^+ p \to \Sigma^+ p$ are allowed as the products are the same as the reactants. Here, the the $\Sigma^- p \to \pi^0 n$ channel of the Σ proton scattering must be taken into consideration to account for all allowed states, as the coefficients of these state will affect the σ-ratio of $\Sigma^+ p$ and $\Sigma^- p$.

The final state of the reaction and the CG-coefficients can be found from the PDG table for each of the Σp scattering reactions. A more detailed description on the table and how it can be used to determine the CG coefficients can be found on [43] as this is out of the scope of this analysis.

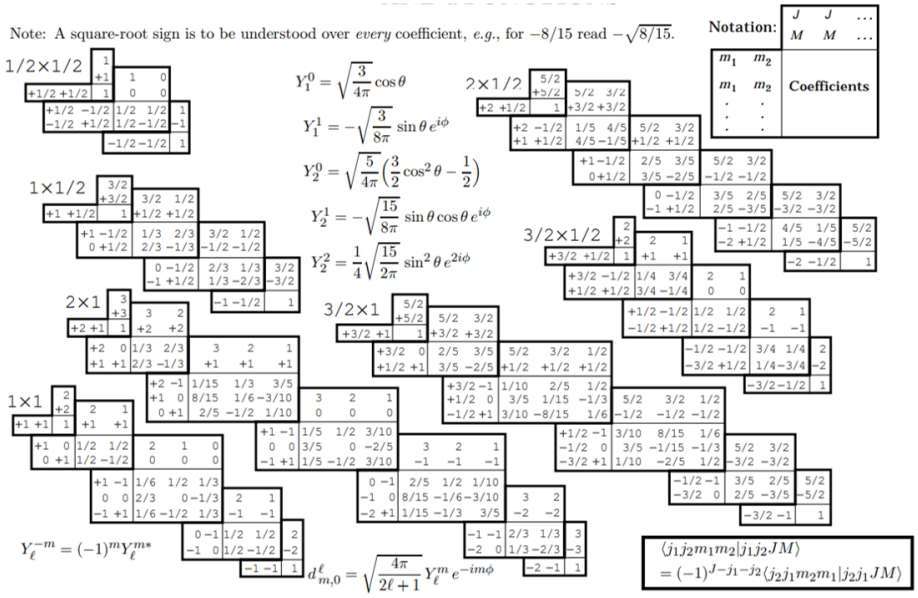

Figure 32: Clebsch-Gordan coefficient tables from PDG [44].

The reaction can be written in terms of the total isospin states and CG-coefficients.

$\Sigma^+ p \to \Sigma^+ p \Rightarrow |1,1\rangle|\frac{1}{2},\frac{1}{2}\rangle = |\frac{3}{2},\frac{3}{2}\rangle$

$\Sigma^- p \to \Sigma^- p \Rightarrow |1,-1\rangle|\frac{1}{2},\frac{1}{2}\rangle = \sqrt{\frac{1}{3}}|\frac{3}{2},\frac{-1}{2}\rangle - \sqrt{\frac{2}{3}}|\frac{1}{2},\frac{-1}{2}\rangle$

$\Sigma^- p \to \Sigma^0 n \Rightarrow |1,0\rangle|\frac{1}{2},\frac{-1}{2}\rangle = \sqrt{\frac{2}{3}}|\frac{3}{2},\frac{-1}{2}\rangle + \sqrt{\frac{1}{3}}|\frac{1}{2},\frac{-1}{2}\rangle$

6.1.3 Cross Section ratio determination using Isospin and CG-coefficients

In order to determine the cross-section ratio using the Isospin states and the subsidiary coefficients, Fermi's Golden Rule must be employed. Fermi Golden rule states that the cross section of an interaction is proportional to the square of the matrix element of the perturbation Hamiltonian H, between the final f, and initial states I.

$\sigma \propto |\langle f|H|I\rangle|^2$

If the Hamiltonian conserves the isospin and hence the reaction takes place via the strong interaction, the initial and final states must have the same I and I_z.

By calculating the square of Σp interactions the matrix element and taking the ratio of the reactions we can find the cross-section ratio.

Lets begin by representing each interaction as a matrix element along with the appropriate CG-coefficient,

$$\Sigma^+ p \to \Sigma^+ p = \langle \frac{3}{2}, \frac{3}{2} | H | \frac{3}{2}, \frac{3}{2} \rangle \tag{51}$$

$$\Sigma^- p \to \Sigma^- p = \frac{1}{3}\langle \frac{3}{2}, \frac{-1}{2} | H | \frac{3}{2}, \frac{-1}{2} \rangle + \frac{2}{3}\langle \frac{1}{2}, \frac{-1}{2} | H | \frac{1}{2}, \frac{-1}{2} \rangle = \frac{1}{3}\langle \frac{3}{2}, \frac{-1}{2} | H | \frac{3}{2}, \frac{-1}{2} \rangle \tag{52}$$

The first term in eq. 52, represents the contribution of the Σ^- particle in the final state with I and I_z $\left(\frac{3}{2}, \frac{-1}{2}\right)$ respectively.

If the Σ^- and the proton form a bound state with total isospin of I = 3/2 , then only the components with total I =3/2 will contribute significantly to the scattering interaction. This is due to the fact that the strong interaction will favour this isospin configuration. The $\frac{2}{3}\langle \frac{1}{2}, \frac{-1}{2} | H | \frac{1}{2}, \frac{-1}{2} \rangle$ can therefore be neglected as it will not be favoured by the strong interaction.

$$\begin{aligned} \Sigma^- p \to \Sigma^0 n &= \sqrt{\frac{1}{3}}\sqrt{\frac{2}{3}}\langle \frac{3}{2}, \frac{-1}{2} | H | \frac{3}{2}, \frac{-1}{2} \rangle - \sqrt{\frac{1}{3}}\sqrt{\frac{2}{3}}\langle \frac{1}{2}, \frac{-1}{2} | H | \frac{1}{2}, \frac{-1}{2} \rangle \\ &= \frac{\sqrt{2}}{3}\langle \frac{3}{2}, \frac{-1}{2} | H | \frac{3}{2}, \frac{-1}{2} \rangle \end{aligned} \tag{53}$$

In strong interactions, contributions from states with lower isospin, such as the second term in Equation 53 involving $\frac{1}{2}$ isospin, are less preferred for higher isospin configurations.

The cross section will be proportional to the square of the coefficients of each reaction. The ratios of the Σ interactions are given by,

$\sigma_{\Sigma^+ p \to \Sigma^+ p} = 1$

$\sigma_{\Sigma^- p \to \Sigma^- p} = \frac{1}{9}$

$\sigma_{\Sigma^- p \to \Sigma^0 n} = \frac{2}{9}$

The cross section ratio of the 3 reactions is given by,

$\sigma_{\Sigma^+ p \to \Sigma^+ p} : \sigma_{\Sigma^- p \to \Sigma^0 n} : \sigma_{\Sigma^- p \to \Sigma^- p} = 9 : 2 : 1$

The ratio of $\sigma_{\Sigma^+ p}$ to $\sigma_{\Sigma^- p}$ is determined by,

$$\frac{\sigma_{\Sigma^+ p}}{\sigma_{\Sigma^- p}} = \frac{\sigma_{\Sigma^+ p \to \Sigma^+ p}}{\sigma_{\Sigma^- p \to \Sigma^0 n} + \sigma_{\Sigma^- p \to \Sigma^- p}} = 3 \tag{54}$$

6.2 Comparison with Experimental Cross Section Ratio

Now that the cross section ratio was determined using the CG-coefficients, it can be employed for comparisons with the experimental results. Figure 33 illustrates that there is a level of agreement between experimental and theoretical predictions. However, it shall be noted, that CG-coefficients are more appropriately used for determining cross sections of low energy strong interaction scattering events. At higher energies additional contributing mechanisms that will lead to a deviation from the predicted value. From figure 33 it can be observed that as the momentum increases there is a larger deviation of the experimental results from the theoretical.

Using a Kernel density function, the distribution of the cross section ratios was illustrated(see fig 34). A Gaussian kernel, also known as the normal distribution, was utilized.

The Gaussian kernel function is defined as:

$$K(x) = \frac{1}{\sqrt{2\pi}} e^{-\frac{x^2}{2}} \tag{55}$$

where x represents the difference between the point of interest and the data point. The Gaussian kernel function assigns weights to data points based on their proximity to each individual data point. Closer data points receive higher weights.

It can be observed that all cross section ratios fall within 1 standard deviation from the mean, with the exception of the "dip" value and the ratio at 0.6-0.7 GeV/c. Furthermore, the theoretical prediction of the ratio ($\frac{\sigma_{\Sigma^+ p}}{\sigma_{\Sigma^- p}} = 3$) falls within 1σ from the mean. This provides a good preliminary agreement of the experimental and theoretical results.

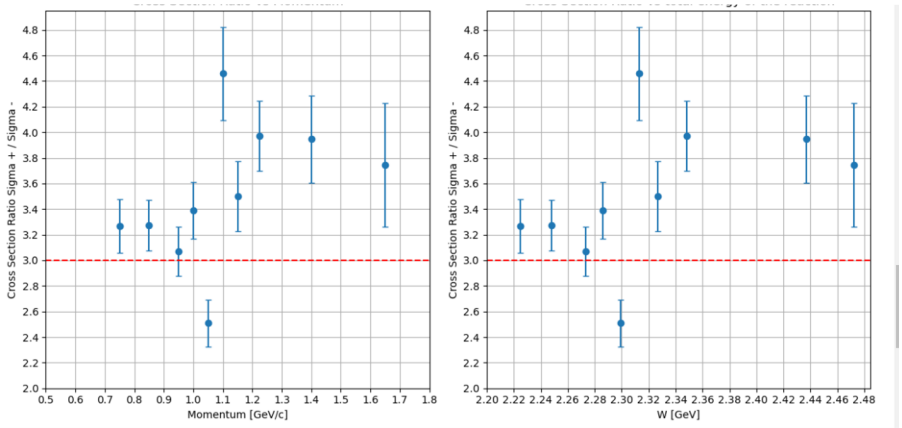

Figure 33: Experimental cross section ratio against momentum p (left), and total energy of the reaction W(right), plotted together with the cross section prediction from the CG-coefficients (red).

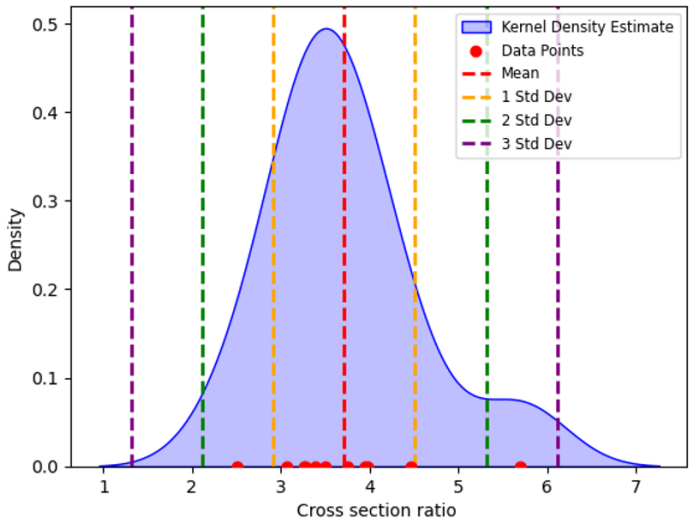

Figure 34: Kernel density function of the distribution of the cross section ratios, with $\mu = 3.712028478$ and $\sigma = 0.8392480417$. Most data fall within 1σ from the mean.

.

6.3 Conclusions

The work presented in this analysis examined the hyperon-nucleon interactions between Σ^+ and Σ^- baryon and the proton using the data collected by the

CLAS detector during the g12 experiment carried out at the Thomas Jefferson National Accelerator Facility and using the theoretical prediction using the Clebsch-Gordon coefficients of the Isospin.

Prior to this analysis the data available for the aforementioned scattering interactions were notably scarce. It is true that this project did not yield results of very high precision that may be taken as the definitive cross sections of the $\Sigma^- p \to \Sigma^- p$ and $\Sigma^+ p \to \Sigma^+ p$ scattering interactions. However,the fact that the cross section ratios at low momenta seem to fall into broad agreement with the theoretical predictions from the Clebsch-Gordon coefficients can be viewed as a promising preliminary finding. This the first stepping-stone for the analysis of the Σp hyperon-nucleon interactions, and future work must be done in order to extract more accurate results of the cross section ratios.

The next step for a future experimental analysis, shall be the determination of the actual acceptance of the detector as well. Additionally, a more time-consuming but more efficient and realistic simulation should be performed in order to obtain more accurate path lengths of the reaction and therefore more accurate cross sections. Both of these procedures can be done with utilisation of GSIM. This will allow the calculation of the individual cross sections of Σ^+ and Σ^-.

Further theoretical analysis that will include not only the cg-coefficients method but a variety of models, more suited to predict cross-section ratios at higher energies shall be employed. This will allow for comparison with the experimental results at a bigger spectrum.

Finally, this work may help gain insight in the hyperon-nucleon interactions, by providing a foundational understanding of the interaction of Σ^+ and Σ^- baryons with protons. By validating theoretical models with experimental data, this research will assist the collaboration of experimentalists and theorists, in the attempt of solving the Hyperon puzzle of Neutron Stars.

A Appendix A

Table 1: Table of Experimental Data: Momentum bin in GeV/c, W (total energy of the reaction) in GeV, Cross Section Ratio of Σ^+ to Σ^-, and the corresponding error in the ratio.

Momentum Range	**W**	σ^+/σ^-	**Error in the Ratio**
0.6-0.7	2.203338976	5.70179805	0.705966
0.7-0.8	2.22476967	3.265272744	0.209036
0.8-0.9	2.248120643	3.273730691	0.197592
0.9-1.0	2.273102848	3.068300596	0.190467
0.95-1.05	2.28612232	3.390405947	0.221803
1.0-1.1	2.299453111	2.509805951	0.1834
1.05-1.15	2.313066793	4.459755712	0.363266
1.1-1.2	2.326936743	3.498766808	0.273745
1.15-1.3	2.348168278	3.973754078	0.272855
1.3-1.5	2.437092737	3.947087393	0.341561
1.5-1.8	2.472209738	3.743635286	0.481894

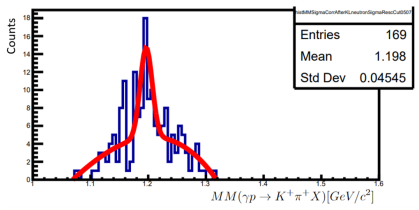

(a) 0.6-0.7 GeV/c

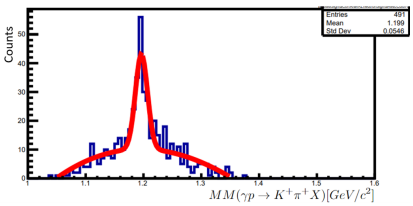

(b) 0.7-0.8 GeV/c

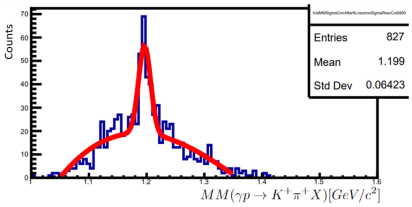

(c) 0.8-0.9 GeV/c

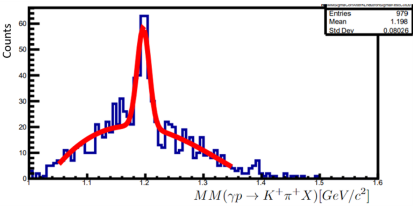

(d) 0.9-1.0 GeV/c

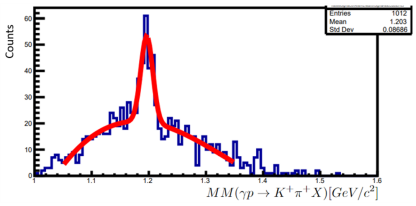

(e) 0.95-1.05 GeV/c

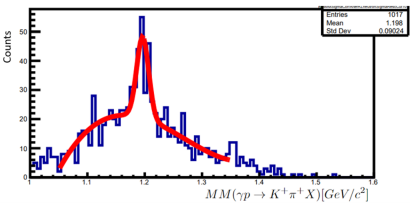

(f) 1.0-1.1 GeV/c

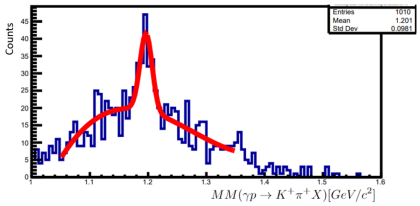

(g) 1.05-1.15 GeV/c

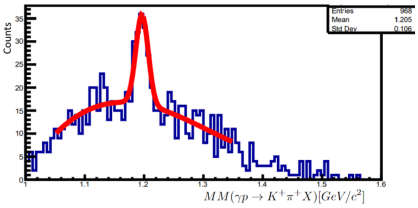

(h) 1.1-1.2 GeV/c

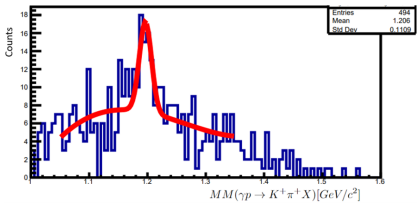

(i) 1.15-1.3 GeV/c

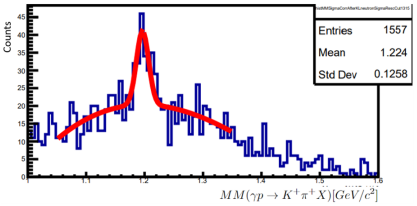

(j) 1.3-1.5 GeV/c

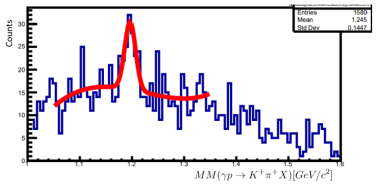

(k) 1.5-1.8 GeV/c

Figure 35: Missing mass distribution plot for Σ^-.

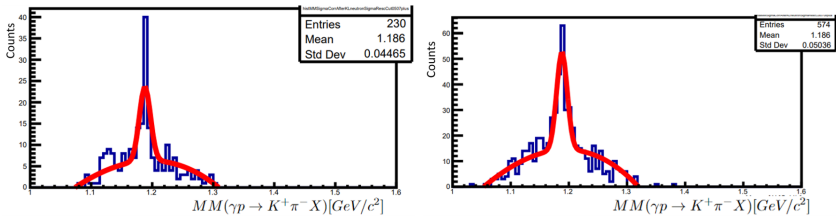

(a) 0.6-0.7 GeV/c

(b) 0.7-0.8 GeV/c

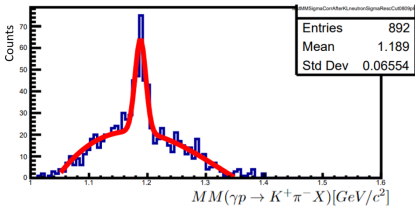

(c) 0.8-0.9 GeV/c

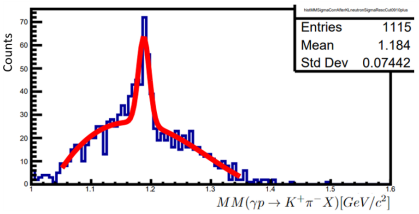

(d) 0.9-1.0 GeV/c

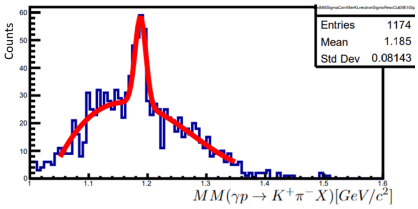

(e) 0.95-1.05 GeV/c

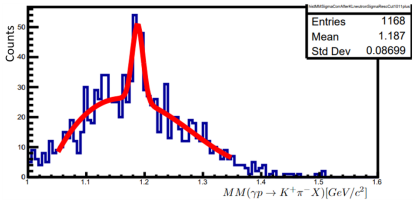

(f) 1.0-1.1 GeV/c

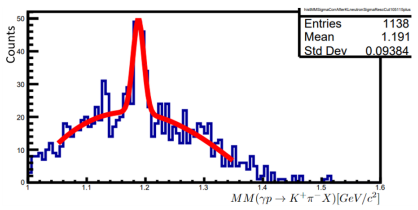

(g) 1.05-1.15 GeV/c

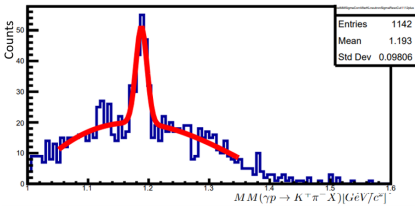

(h) 1.1-1.2 GeV/c

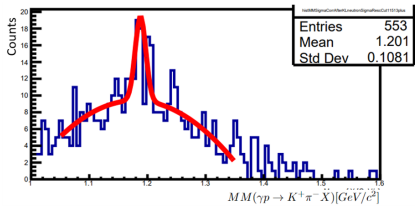

(i) 1.15-1.3 GeV/c

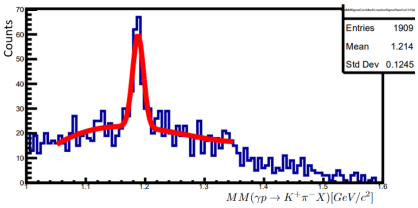

(j) 1.3-1.5 GeV/c

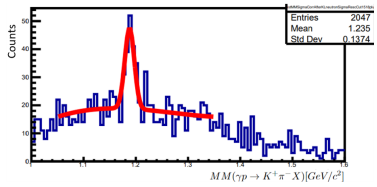

(k) 1.5-1.8 GeV/c

Figure 36: Missing mass distribution plot for Σ^+.

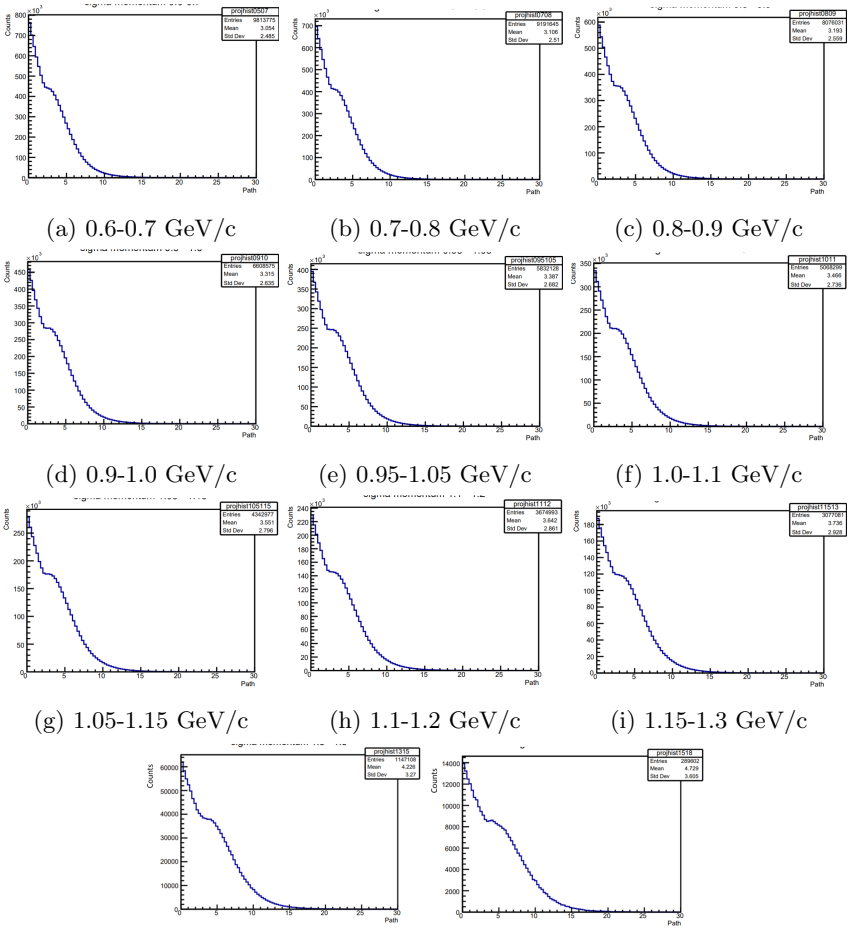

(a) 0.6-0.7 GeV/c (b) 0.7-0.8 GeV/c (c) 0.8-0.9 GeV/c

(d) 0.9-1.0 GeV/c (e) 0.95-1.05 GeV/c (f) 1.0-1.1 GeV/c

(g) 1.05-1.15 GeV/c (h) 1.1-1.2 GeV/c (i) 1.15-1.3 GeV/c

(j) 1.3-1.5 GeV/c (k) 1.5-1.8 GeV/c

Figure 37: Path length distribution of Σ^- in cm.

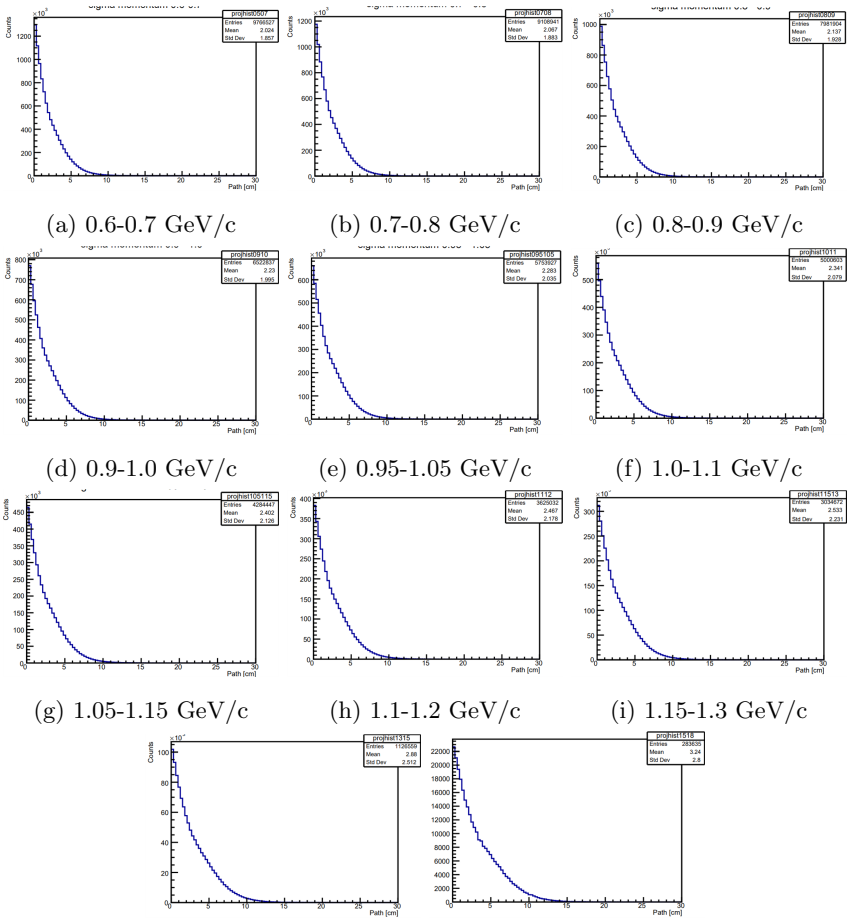

(a) 0.6-0.7 GeV/c (b) 0.7-0.8 GeV/c (c) 0.8-0.9 GeV/c

(d) 0.9-1.0 GeV/c (e) 0.95-1.05 GeV/c (f) 1.0-1.1 GeV/c

(g) 1.05-1.15 GeV/c (h) 1.1-1.2 GeV/c (i) 1.15-1.3 GeV/c

(j) 1.3-1.5 GeV/c (k) 1.5-1.8 GeV/c

Figure 38: Path length distribution of Σ^+ in cm.

B References

References

[1] Discovery of electrons Encyclopedia Britannica. Encyclopedia Britannica, inc. Available at: https://www.britannica.com/science/atom/Discovery-of-electrons (Accessed: March 14, 2023).

[2] Joseph John "J. J." Thomson (2022) Science History Institute. Available at: https://www.sciencehistory.org/historical-profile/joseph-john-j-j-thomson (Accessed: March 15, 2023).

[3] Dahl, P.F. (1997) "p.324," in Flash of the cathode rays: A history of J.J. Thomson's Electron. Bristol: Institute of Physics.

[4] Rutherford, E. (1911) "LXXIX. the scattering of α and β particles by matter and the structure of the atom," The London, Edinburgh, and Dublin Philosophical Magazine and Journal of Science, 21(125), pp. 669–688. Available at: https://doi.org/10.1080/14786440508637080.

[5] Kragh, H. (2012) Niels Bohr and the quantum atom: The Bohr model of atomic structure 1913-1925. Oxford Uni.

[6] Libretexts (2023) 10.4: The Bohr model, Chemistry LibreTexts. Libretexts. Available at: https://chem.libretexts.org/Courses/AnokaRamsey_Community_College/Introduction_to_Chemistry/10%3A_Electrons_in_Atoms/10.04%3A_The_Bohr_Model (Accessed: March 23, 2023).

[7] Gearhart, C.A. (2014) "The franck-hertz experiments, 1911–1914 experimentalists in search of a theory," Physics in Perspective, 16(3), pp. 293–343. Available at: https://doi.org/10.1007/s00016-014-0139-3.

[8] Bohr model (2023) Encyclopædia Britannica. Available at: https://www.britannica.com/science/Bohr-model (Accessed: 08 December 2023).

[9] The nobel prize in physics 1963 (7 Dec 2023) NobelPrize.org. Available at: https://www.nobelprize.org/prizes/physics/1963/ceremony-speech/(Accessed:07December2023).

[10] http://hyperphysics.phy-astr.gsu.edu/hbase/Nuclear/shell.html

[11] Oerter, R. (2006) The theory of almost everything: The standard model, the unsung triumph of modern physics. New York: Pi Press.

[12] The nobel prize in physics 1963 (no date) NobelPrize.org. Available at: https://www.nobelprize.org/prizes/physics/1963/ceremony-speech/ (Accessed: 07 December 2023).

[13] Iliopoulos, J. and Tomaras, T.N. (2021) Elementary particle physics: The standard theory. New York, NY: Oxford University Press.

[14] B. Carithers; P. Grannis (1995). "Discovery of the Top Quark". Beam Line.

[15] M., W.S.S. (1998) Introductory nuclear physics. N.Y.: Wiley & Sons.

[16] Tarek Abouelfadl Mohamed, A. (2020). The Standard Model of Particle Physics. In: Measurement of Higgs Boson Production Cross Sections in the Diphoton Channel. Springer Theses. Springer, Cham. https://doi.org/10.1007/978-3-030-59516-6_1

[17] Jackson, J.D., Gove, H.E. and Schwitters, R.F. (1982) Annual Review of Nuclear and Particle Science. Palo Alto, CA: Annual Reviews Inc. p.177 – 209.

[18] Köhn, C., & Ebert, U. (2014). The structure of ionization showers in air generated by electrons with 1 MeV energy or less. Plasma Sources Science and Technology, 23(4), 045001.

[19] CERN accelerating science (no date) CERN. Available at: https://home.cern/ (Accessed: 13 December 2023).

[20] Introduction to elementary particles (1971). John Wiley.

[21] Gell-Mann, M. (1953) "Isotopic spin and new unstable particles," Physical Review, 92(3), pp. 833–834. Available at: https://doi.org/10.1103/physrev.92.833.

[22] Degrange, B., Fontaine, G. and Fleury, P. (2013) "Tracking Louis Leprince-Ringuet's contributions to cosmic-ray physics," Physics Today, 66(6), p. 8. Available at: https://doi.org/10.1063/pt.3.1989.

[23] Tolos, L. and Fabbietti, L. (2020) "Strangeness in nuclei and neutron stars," Progress in Particle and Nuclear Physics, 112, p. 41. Available at: https://doi.org/10.1016/j.ppnp.2020.103770.

[24] Seeds, M.I.A. (2005) Astronomy: The solar system and beyond. Australia: Thomson Brooks/Cole Publishing Company. p. 339

[25] Hewish, A. et al. (1968) "Observation of a rapidly pulsating radio source," Pulsating Stars, pp. 5–9. Available at: https://doi.org/10.1007/978-1-4899-6387-1_1.

[26] Chatterjee, D. and Vidaña, I. (2016) "Do hyperons exist in the interior of neutron stars?," The European Physical Journal A, 52(2). Available at: https://doi.org/10.1140/epja/i2016-16029-x.

[27] Schaffner-Bielich, J. et al. (2002) "Phase transition to hyperon matter in neutron stars," Physical Review Letters, 89(17). Available at: https://doi.org/10.1103/physrevlett.89.171101.

[28] R. S. Lynch et al. The Green Bank Telescope 350 mhz drift-scan survey ii: Data analysis and the timing of 10 new pulsars, including a relativistic binary. The Astrophysical Journal, 763:81, 01 2013.

[29] Collaboration, C. et al. (2021) Improved Λp elastic scattering cross sections between 0.9 and 2.0 Gev/c and connections to the neutron star equation of State, arXiv.org. Available at: https://arxiv.org/abs/2108.03134 (Accessed: 08 December 2023).

[30] B. A. Mecking et al. The CEBAF large acceptance spectrometer (CLAS). Nuclear Instruments and Methods in Physics Research Section A: Accelerators, Spectrometers, Detectors and Associated Equipment, 503(3):513–553, 2003

[31] Sober D. I. et al. The bremsstrahlung tagged photon beam in Hall B at JLab. Nuclear Instruments and Methods in Physics Research Section A: Accelerators, Spectrometers, Detectors and Associated Equipment, 440(2):263–284, 2000

[32] Y. G. Sharabian et al. A new highly segmented start counter for the CLAS detector. Nuclear Instruments and Methods in Physics Research Section A: Accelerators, Spectrometers, Detectors and Associated Equipment, 556(1):246–258, 2006.

[33] M. D. Mestayer et al. The CLAS drift chamber system. Nuclear Instruments and Methods in Physics Research Section A: Accelerators, Spectrometers, Detectors and Associated Equipment, 449(1-2):81–111, 2000.

[34] E. S. Smith et al. The time-of-flight system for CLAS. Nuclear Instruments and Methods in Physics Research Section A: Accelerators, Spectrometers, Detectors and Associated Equipment, 432(2-3):265–298, 1999.

[35] M. Amarian et al. The CLAS forward electromagnetic calorimeter. Nuclear Instruments and Methods in Physics Research Section A: Accelerators, Spectrometers, Detectors and Associated Equipment, 460(2-3):239–265, 2001.

[36] S. Stepanyan et al. Energy calibration of the hall b bremsstrahlung tagging system using a magnetic pair spectrometer. CLAS-Note, 012, 2005.

[37] P. Mattione, Kinematic Fitting of Detached Vertices, M.S. Thesis, Rice University (2007).

[38] Zachariou N. (2012). Determination of the Azimuthal Asymmetry of Deuteron Photodisintegration in the Energy Region $E_\gamma = 1.1 - 2.3GeV$. [Doctoral dissertation, The George Washington University, The Columbian College of Arts and Sciences].

[39] Chetry, T. (2019). A Study of the Reaction $\gamma d \rightarrow \pi^+\pi^- d$ (From Vector Mesons to Possible Dibaryons). [Master's thesis, College of Arts and Sciences, Ohio University].

[40] JLab 2019, 'GSIM Documentation', Jefferson Lab Hall B, Available at: https://www.jlab.org/Hall-B/document/gsim/node1.html (Accessed: 11 December 2023).

[41] Dash, T. and Acharya, A. (2017) 'RATIO OF CROSS SECTIONS OF ELEMENTARY STRONG REACTIONS USINGnbsp; CLEBSCH GORDON (CG) CO-EFFICIENTS', INTERNATIONAL JOURNAL OF ENGINEERING SCIENCES and RESEARCH TECHNOLOGY [Preprint]. doi:10.5281/zenodo.808972 .

[42] Nakano, T. and Nishijima, K. (1953) 'Charge independence forv-particles', Progress of Theoretical Physics, 10(5), pp. 581–582. doi:10.1143/ptp.10.581.

[43] Phys30201 mathematical fundamentals of Quantum ... - theoretical physics. Available at: `https://www.theory.physics.manchester.ac.uk/~judith/Quantum/pdg-clebsch.pdf` (Accessed: 11 December 2023).

[44] 34.CLEBSCH-gordan coefficients,sphericalharmonics ... - particle data group. Available at: https://pdg.lbl.gov/2002/clebrpp.pdf (Accessed: 11 December 2023).

[45] Pauli, W. (2000), 'Wave Mechanics', Pauli Lectures on Physics (Dover Books on Physics), Dover Publications, ISBN 0486414620, pp. 150–151